

Protein Co-Enrichment Analysis of Extracellular Vesicles

Molly L. Shen^{1,2}, Zijie Jin^{1,2,†}, Rosalie Martel^{1,2,†}, Andreas Wallucks^{1,2}, Lucile Alexandre^{1,2},
Philippe DeCorwin-Martin^{1,2}, Lorena Oliveira Fernandes de Araujo^{1,2}, Andy Ng^{1,2}, David
Juncker^{1,2,*}

¹Biomedical Engineering Department, McGill University, Montreal, QC, Canada

²McGill University & Genome Quebec Innovation Centre, McGill University, Montreal, QC, Canada

[†] Z.J. and R.M. contributed equally.

Abstract:

Extracellular vesicles (EVs) carry a variety of cell-derived proteins that confer functionality and selective cell uptake. However, whether proteins are packaged stochastically or co-enriched within individual EVs, and whether co-enrichment fluctuates under homeostasis and disease, has not been measured. EV abundance and protein global relative expression have been qualified by bulk analysis. Co-enrichment, which occurs within individual EVs, is not directly accessible via bulk measurement and has not been reported for single EV analysis. Here, we introduce the normalized index of co-enrichment (NICE) of proteins to measure co-enrichment. NICE was derived by (i) capturing EVs based on the expression of a membrane-bound protein, (ii) probing for the co-expression of a second protein at the population level—EV integrity underwrites the detection of single EV co-expression without the need to resolve single EVs—and (iii) normalizing measured values using two universal normalization probes. The two universal probes capture ‘all’ EVs and detect ‘all’ EVs, respectively. Axiomatically, $NICE = 1$ for stochastic inclusion or no overall co-enrichment, while for positive and negative co-enrichment $NICE > 1$ or < 1 , respectively. Using antibody microarrays, we quantified the NICE of tetraspanins, growth factor receptors and integrins in EVs from the cell supernatant of eight breast cancer cell lines of varying metastatic potential and organotropism, combinatorically mapping up to 104 protein pairs simultaneously. Our analysis revealed protein enrichment and co-expression patterns consistent with previous findings. For the organotropic cell lines, most protein pairs were co-enriched on EVs, with the majority of NICE values between 0.2 to 11.5, and extending from 0.037 to 80.4. Median NICE were either negative, neutral or positive, depending on the cells. NICE analysis is easily multiplexed and is compatible with microarrays, bead-based and single EV assays. Additional studies are needed to deepen our understanding of the potential and significance of NICE for research and clinical uses.

1. Introduction:

Extracellular vesicles (EVs) are membrane-derived, cargo-carrying vesicles secreted by all cell types that are found in various body fluids and have attracted large amounts of interest after it was shown numerous times that they serve as a bona fide communication system in the body.¹⁻⁵ EVs are transported via the blood circulatory system and their extensive involvement in health and disease makes them an attractive source of biomarkers for liquid biopsy,⁶⁻⁸ as well as vehicles for drug delivery.^{9,10} EV subpopulations are characterized by their size, composition, or cargo (i.e. RNA and proteins), which determines their biological function and clinical significance.¹¹⁻¹⁴ The expression of various cargo is commonly normalized to the sample size, which in bulk analysis can be the total protein concentration or amount of housekeeping gene products, and in single EV analysis methods is the total EV count.¹⁵ This normalized cargo detection signal, which we refer to as global relative expression (GRE), is the average abundance of the target protein in the whole EV population and can easily be compared between experiments. From measurements like these, it is known that proteins may be over- or under-expressed compared to a baseline, for example when comparing the GRE between a pathological condition and a healthy, homeostatic state.

The co-expression of pairs or proteins, and even larger sets of proteins in EVs are now being measured and shed new light on the complexity and variability of EV cargo. Co-expression of proteins can be established by co-detecting proteins via immunofluorescence on individual EVs or in sandwich antibody binding assays or in proximity ligation assays on antibody-captured EV subpopulations.¹⁶⁻¹⁸ Since proteins can interact both directly through physical binding and indirectly by being part of common or related pathways leading to their co-packaging in EVs, co-expression patterns might help resolve many open questions such as EV classes and roles in communication, identify EV subpopulations with unique proteomic signatures, link EV cargo to biogenesis pathways by co-detecting protein components of the cargo selection machinery, and elucidate how tightly cells control EV cargo packaging in general.¹⁹

Note that owing to the microscopic size of EVs, only a limited number of proteins may be expressed in any given EV, and most proteins are only expressed in a small subset of the EV population. As a result, it is thus feasible, and indeed now common, to define EV populations by the expression of a particular protein, i.e., say the EV subpopulation that expresses the protein B , as the subpopulation B . When we measure the co-expression of a second protein, say protein A , within the EV subpopulation that expresses protein B , it should be possible to compare the

expression of A within the subpopulation B to the expression of A within the entire population of EVs. An important prerequisite is to quantify the total EV numbers within the whole population and the subpopulation B , and use it to normalize the expression of protein A within the subpopulation and within the entire population, with the latter being the GRE^A . With relative expression measurements available, it should be possible to calculate whether the relative co-expression of A in the subpopulation B is similar, or less, or higher than the GRE^A . The measurement of changes in the co-expression of A in the subpopulation B relative to the GRE^A would have the potential to further biological insights. Moreover, as described above for the expression of proteins in EVs, the co-expression of pairs or larger numbers of proteins in different EV subpopulations under different states and conditions of homeostasis and disease could also help illuminate new aspects distinguishing these states, and help generate new hypotheses and potentially uncover mechanisms and biomarkers to study, understand and characterize physiological states. Extracting and comparing the information about co-expression of proteins in EVs requires a method to establish the GRE and the relative co-expression of proteins in a manner that is comparable to enable normalization. While GRE is readily quantifiable with various methods, it is not amenable to measure co-expression, and hence other approaches are needed. Armed with comparable measurements, an algorithm and quantitative metric of relative co-expression that can be readily interpreted are needed.

Here, we introduce the concept of co-enrichment of proteins within EVs that is quantified by the normalized index of co-enrichment (NICE), which is readily interpretable. NICE is derived based on measuring (i) the protein expression signal in the whole EV population and (ii) the co-expression signal in a protein-defined subpopulation, (ii) normalizing each based on EV abundance to obtain the GRE and the relative co-expression (RCE), respectively, and finally (iv) dividing the RCE by the GRE value that yields NICE. Using an antibody microarray, we establish the experimental workflow to determine the GRE and the pairwise RCE for multiple protein pairs, simultaneously using ‘universal’ calibrants for normalization. We measured the GRE of tens of proteins, the pairwise RCE of over one hundred protein pair combinations in a single experiment, and calculated NICE for each. GRE, RCE, and NICE were derived for canonical EV markers and cancer-associated proteins in EVs purified from breast cancer cells of varying metastatic potential and organotropism, and variations in NICE observed depending on cell, protein-pair and

organotropism. We validated detection by NICE using protein dimers as well as protein pairs with reported association and found new co-enrichment patterns that warrant further investigation.

2. **Results:**

2.1 **A Note on the Mathematical Formalism of co-enrichment**

Co-enrichment between two protein cargos A and B is analyzed by considering the distribution of a given protein A in the total EV population, and evaluating whether the distribution is different in a subpopulation of EVs that co-express the second protein B . In other words, it is the conditional enrichment of A given co-detection of B on the same EV. While the distribution of A can be arbitrarily complex in principle, the experimentally most readily detected changes concern the concentration of A (i.e., how many copy numbers of A are present on average in EVs expressing the protein B written as B^+ EVs).

Conceptually, we define $\bar{N}(A)$ as the concentration of A in the total population, which is the total copy number of protein A divided by the total number of EVs in the sample (i.e., population size, and which is equivalent to the GRE^A measured experimentally). Similarly, $\bar{N}(A|B^+)$ measures the conditional concentration of A in the B^+ subpopulation, i.e., the subpopulation of EV that express at least one copy of B . It is obtained by dividing the number of protein A on B^+ EVs by the total number of B^+ EVs. Concentration co-enrichment of protein A in the B^+ subpopulation can then be scored as

$$\text{NICE}_B^A = \frac{\bar{N}(A|B^+)}{\bar{N}(A)}$$

A $\text{NICE}_B^A > 1$ score indicates that the B^+ subpopulation is co-enriched in protein A compared to the whole EV population from that sample and implies a strong correlation between the two proteins. Conversely, a $\text{NICE}_B^A < 1$ score indicates that B^+ subpopulation is depleted of A , as the concentration of A in B^+ EVs are less than the overall concentration of A in the entire EV population. Creating co-enrichment maps between multiple pairs of proteins from the same EV sample thus allows to investigate the correlation between the EV cargo that is not distinct from simple co-expression data, i.e., $\bar{N}(A|B^+)$.

We note that NICE as defined here is assumed to be asymmetric, i.e., $\text{NICE}_B^A \neq \text{NICE}_A^B$, since subpopulation selection (i.e., antibody-captured EVs) does not distinguish whether one or multiple copies of the protein are present whereas the concentration measurement of the other

protein does. We also note that other metrics to score co-enrichment between two proteins are possible. For example, $NICE_B^A$ is by itself not indicative of whether the B^+ subpopulation necessarily contains more than one copy of A in every single B^+ EVs, or whether it is enriched in a small subset of B^+ EV which highly express A . Thus, an alternative definition could include the change of the frequency per EV by which A is detected in the overall and the B^+ subpopulation (see discussion for more details). However, realistically, given the promiscuity in cargo sorting mechanisms and the known overlap between protein cargo of EV subtypes (e.g., exosomes vs small ectosomes), we posit that such different co-enrichment scores are likely correlated in most scenarios. In this work, we show a proof of principle demonstration of co-enrichment analysis using the concentration-defined co-enrichment as illustrated above, which lends itself to high throughput subpopulation analysis using antibody microarrays and goes beyond the more common co-expression analysis.

2.2 NICE Analysis of Proteins in EVs Using Antibody Microarrays

We determined $NICE_B^A$ using antibody microarrays to quantify pairwise protein co-enrichment within an EV population. We circumvented the need to resolve single EVs by using a capture and detection sandwich geometry which readily selects the B^+ subpopulation for any target protein B . The concentration $\bar{N}(A|B^+)$ of A within this subpopulation was assessed using immunofluorescence detection. This measurement was compared to the total abundance $\bar{N}(A)$ of A in the whole population which is facilitated by introducing a universal capture surface. The universal capture of EVs is based on T-cell immunoglobulin domain and mucin domain-containing protein 4 (TIM4) and its high affinity binding to phosphatidylserine, which is present on the membrane bilayer of EVs of cancer origin, and are the focus of this study.²⁰ For our experiments, we posit that EVs captured by TIM4 are representative of the entire EV population and that capture is independent of specific protein expression, which we confirmed experimentally in the HT29 human colorectal adenocarcinoma cell line used in our validation experiments. Using the universal capture TIM4 or a specific antibody to capture a subpopulation bearing the targeted protein, we provide experimental data in support of the universality of labeling and capture probes below.

Importantly, both measures of the concentration of A needed to be further normalized to the respective populations in which they were measured. To this end we used ‘universal’ detection labels, namely cell tracker dyes (CTD), or biotinylation and fluorescent streptavidin, to provide a

measure of the number of EVs immobilized on the surface. Universal in our context is aspirational and a functional property in the context of our workflow, and we provide limited evidence for universality for our examples.

The full workflow to capture and detect EVs and measure the expression of proteins, along with the algorithm to compute NICE, are illustrated in Figure 2. Microarrays patterned with capture antibodies (i.e., anti-protein B antibodies) and TIM4 were incubated with cell tracker dye (CTD)-labeled EVs. Next, the EVs were incubated with biotinylated detection antibodies (e.g., anti-protein A antibodies) followed by fluorescent streptavidin. The fluorescence signal of both the CTD and the streptavidin (which was proportional to the expression level of protein A) were quantified with a microarray scanner.

2.3 *NICE Analysis and Calculation*

The fluorescence intensities of the microarray spots were converted into single intensity values for each spot and contain averaged intensities of many EVs. The detection signal of protein A on the TIM4 spot is denoted I_{Σ}^A and is a measurement of the overall abundance of this protein in the total population. I_B^A on the other hand, is the detection signal of protein A on the anti-protein B capture spot, and is thus the un-normalized co-expression value of protein A in the B^+ EV subset/subpopulation. Our workflow used the CTD intensities on TIM4 (I'_{Σ}^{Ω}) and on the protein B capture spot (I'_{B}^{Ω}) to normalize these values to their respective population and subpopulation size. This was strictly necessary to control for different capture rates of the affinity binders and the fact that the B^+ subpopulation might be small and hence fewer EVs are captured. Here, the intensity of the universal CTD is noted I' (as opposed to I) to reflect the use of distinct fluorescent dyes, which precludes direct comparison of the resulting intensities (see Table I for additional explanations and nomenclature). We define the normalized global relative expression of protein A as

$$\text{GRE}^A = \frac{I_{\Sigma}^A}{I'_{\Sigma}^{\Omega}} \quad (1)$$

and the relative expression of A given B as

$$\text{RCE}_B^A = \frac{I_B^A}{I'_{B}^{\Omega}}. \quad (2)$$

GRE^A thus reflects the normalized expression of protein A in the entire EV population, while RCE_B^A reflects the normalized pairwise co-expression of protein A in the B^+ subpopulation,

and both can be directly compared. The pairwise co-enrichment score of A given B , or NICE_B^A , is calculated by taking the ratio of RCE_B^A and GRE^A :

$$\text{NICE}_B^A = \frac{\text{RCE}_B^A}{\text{GRE}^A} \quad (3)$$

Note that as the ratio of two expression levels, NICE is unitless and can vary independently from the GRE of the protein, and is unaffected by the different fluorescent yield of Ω . Likewise, as the same detection antibody is used for both GRE and RCE, NICE is not susceptible to variations in fluorescent labeling efficiency as long as the signals reach minimal thresholds.

$\text{NICE}_B^A = 1$ indicates that the proportion of protein A expression is the same in the subpopulation B as in the general EV population when adjusting for the density of captured EVs, and consistent with stochastic inclusion. In contrast, if $\text{NICE}_B^A > 1$ or $\text{NICE}_B^A < 1$, protein A is positively or negatively co-enriched within the EV subpopulation expressing protein B , respectively.

2.4 Validation of CFDA-SE and CTR as Universal Detection Dyes

Fluorescent dyes, such as lipophilic dyes and membrane-permeable organic dyes have been commonly used to visualize and measure EV abundance in bulk and count particles in single EV assays.^{15,21,22} In our study, membrane-permeable organic fluorescent dye Cell Tracker Red (CTR) and the amine-reactive dye 5-(and-6)-Carboxyfluorescein Diacetate Succinimidyl Ester (CFDA-SE) were chosen as candidate universal detection as they are commonly used for non-specific EV labeling,^{22,23} and that they are readily implementable to our assay workflow. N-hydroxysuccinimido biotin (NHS-Biotin)-based EV biotinylation, which is universal, and subsequent detection via fluorescent streptavidin, were used for cross-validation and benchmarking of CFDA-SE and CTR. PKH26, an amphiphilic lipid dye, was considered but not selected due to its tendency to form aggregates and artificially increase the size of vesicles.^{24,25} The labeling of EVs by CFDA-SE, CTR and biotin were compared by capturing EVs on microarrays with antibodies against the three canonical tetraspanins CD81, CD63 and CD9, and measuring the relative expression of each ‘universal’ dye for each subpopulation. Briefly, purified EVs (see Supplementary Figure 1 for experimental details on EV preparation) were biotinylated and dyed with the cell tracker dyes. The samples were captured on the antibody microarray, incubated with fluorescently labelled streptavidin of compatible excitation and emission profile,

and visualized via a microarray scanner. The detected relative fluorescence unit (RFU) signal of the cell tracker dyes and the fluorescent streptavidin are proportional to the density of EVs on the surface. The RFU signal of EVs captured by each anti-tetraspanin antibodies followed a similar trend for all three dyes, as shown in Figure 3A. The relative expression is preserved for each dye, showing representative, non-specific labelling for the 3 tetraspanin subpopulations (Fig. 3B), and suggesting that CFDA-SE and CTR are both suitable as universal detection dyes.

2.5 Validation of TIM4 as Universal Capture Probe

TIM4 is a membrane protein that binds strongly to phosphatidylserine in the presence of calcium.²⁶ TIM4 has been shown to bind and enrich EVs on magnetic beads²⁷ and on solid surfaces in enzyme-linked immunosorbent assay (ELISA).²⁸ TIM4's capture efficiency was benchmarked to NHS-biotinylated-EVs captured on a streptavidin coated surface. Briefly, purified EVs were biotinylated and dyed with CTR, and subsequently captured on the microarray patterned with TIM4-Fc or streptavidin. The captured EV were then profiled for their tetraspanin expression using antibodies against CD81, CD63, and CD9. TIM4 capture lead to much higher RFU signal for all three tetraspanin detection antibodies when compared to streptavidin capture (Fig. 3C), indicating higher capture efficiency of TIM4. The signal ratio of various tetraspanins were nearly identical (Fig. 3D) regardless of capture method, suggesting an unbiased capture by TIM4 compared to biotinylated EVs. When EVs labelled with CTR were captured on a TIM4 and streptavidin surface, a much higher fluorescence signal was again observed for TIM4, ($p < 0.0001$, Fig. 3E). Thus, we conclude that TIM4 is an adequate high affinity, universal capture agent for EVs with exposed phosphatidylserine.

2.6 Pairwise NICE Profile of EVs from T-47D Breast Cancer Cell Line

EVs derived from the commonly studied breast cancer cell line T-47D were profiled using microarrays with 8 capture antibodies in addition to universal capture TIM4, and probed with 13 detection antibodies, each applied on a replicate microarray in a separate well. The capture antibodies targeted EV-associated tetraspanins (CD81, CD63, and CD9), cancer-associated proteins (ADAM10, CD44, CD82, EGFR, and EpCAM) and were supplemented with the universal

capture TIM4. The detection antibodies targeted the same proteins and further included CD81, CD63, CD9, EGFR, and EpCAM as well as 8 additional targets made up of integrin alpha and beta subunits (ITG- α 2, α V, α 5, α 6, β 1, β 3, β 4, and β 5) previously shown to be associated with cancer.²⁹ We found CD9 to be the most highly expressed tetraspanin in T-47D EVs, both by measuring the total number of EVs captured via an anti-CD9 antibody and quantified with a universal dye (I_{CD9}^{Ω} , Fig. 4A), and when probing the EVs immobilized with a universal capture with an anti-CD9 detection antibody (GRE^{CD9} , Fig. 4B). Subpopulations defined by capture antibodies against ADAM10, CD82, and EpCAM were also abundant. We observed high GRE of tetraspanins, as well as integrin subunits such as ITG- α V, β 1, β 3 and β 5. As GRE measures the relative expression of a particular detection protein target within the entire population, it should be directly comparable to common proteomic assays that lyse EVs prior to analysis via mass spectrometry or ELISA. In agreement with mass spectrometry studies³⁰ we also observed low relative GRE of ITG- α 5 along with the high GRE of ITG- β 1.

Figure 4C-E shows pairwise protein combinations for RFU values (denoted as $I_{Capture}^{Detection}$), $RCE_{Capture}^{Detection}$ and $cNICE_{Capture}^{Detection}$ along with the signal-to-noise ratios (SNRs) in SNR heatmaps. The SNR is reported as the height of each of the heatmap squares and helps gauge the credibility of that measurement. The lowest height represents a SNR of 0.5 and under, while the tallest height represents a SNR above 5; $SNR > 3$ (mid-point of its height) could be considered reliable, and thus representing true values for the RFU signals, as well as for RCE and NICE. We observed low RFU values for integrins such as ITG- α 2, ITG- α 5, ITG- α 6, ITG- β 3 and ITG- β 4, (Fig. 4C), and similar RCE values (Fig. 4D). We arbitrarily define NICE as neutral (stochastic) for the range $0.5 \leq NICE \leq 2$. NICE was neutral to moderately positive for all except ITG- β 3, which was negatively co-enriched. Meanwhile ITG- β 3 was negatively co-enriched ($NICE < 0.5$) for most of the capture subpopulations, as shown in Figure 4E. NICE analysis revealed that although all integrin signals were low, only one was negatively co-enriched.

2.7 NICE Profile of EVs derived from Three Different Breast Cancer Cell Lines

Breast cancers are classified clinically based on the expression of the estrogen receptor (ER), the progesterone receptor (PR) and the human epithelial growth factor 2 receptor (HER2).

ER⁺PR⁺HER2⁻ cancers are the most benign, while ER⁻PR⁻HER2⁻ cancers are the most aggressive with the worst outcomes.³¹ We mapped the NICE of proteins in EVs derived from BT549 (ER⁻PR⁻HER2⁻ triple negative), T-47D (ER⁺PR⁺) and MCF-7 (ER⁺PR⁺) breast cancer cell lines. 19 antibodies were microarrayed targeting many cancer-associated integrin subunits.²⁹ The subpopulation signal (denoted as $I'_{\text{Capture}}^{\Omega}$) and GRE for each target are shown in Figure 5A and 4B, respectively. The abundance of each antibody-captured subpopulation varied greatly among the three cell lines, exceeding the signal obtained with TIM4 for some targets. EV subpopulations captured by CD9, ADAM-10, EpCAM and ITG- α V were abundant in both ER⁺PR⁺ T-47D and MCF-7, while the abundance of CD82-captured EVs greatly differed between T-47D and MCF-7. RCE and NICE of the tetraspanins CD81, CD63, and CD9 are shown in Figure 5C and 5D respectively. While GRE^{CD63} varied among the three cell lines, NICE^{CD63}_{Capture} was neutral or positive (but not negative) for all EV subpopulations examined. Meanwhile, GRE^{CD81} was similar among the three cell lines, yet significant variations were seen in RCE^{CD81}_{Capture} and NICE^{CD81}_{Capture} scores (Fig. 5B – D). Notably, we found that integrin-captured subpopulations such as ITG α 2 (NICE^{CD81} _{α 2} = 0.081), ITG α 6 (NICE^{CD81} _{α 6} = 0.057), and ITG β 4 (NICE^{CD81} _{β 4} = 0.29) and CD44-captured subpopulation (NICE^{CD81}_{CD44} = 0.23) were negatively co-enriched with CD81 in only MCF-7 EVs while positively co-enriched in T-47D and BT549 EVs. Meanwhile, NICE^{CD9}_{CD44} (0.060), and NICE^{CD9} _{α 1} (0.12) were also found to be < 1 in MCF-7 EVs only (Fig. 5D). Low ITG- α 5 EV expression in T-47D and MCF-7 have been observed via mass spectrometry in the literature.^{30,32} We observed low density of EVs capture by anti-ITG- α 5 antibodies for both T-47D and MCF-7 (Fig. 5A), consistent with low expression. In EVs of T-47D cells, all three tetraspanins were positively co-enriched with ITG- α 5. Meanwhile ITG- α 5 is preferentially co-enriched with only CD63 in EVs of MCF-7 cells. Expanding on the recent literature observing vast proteomic heterogeneity across tetraspanin-captured EV subpopulations,^{33–35} we also find heterogeneity and unique protein co-enrichment signatures associated with each tetraspanin.

2.8 NICE of EVs from Parental Breast Cancer Cell and its Organotropic Sublines

Integrin expression in EVs has been linked to organotropism of breast cancer metastasis, and notably ITG- α 6 and ITG- β 4 have been associated with lung organotropism.³⁶ Here we set out to

profile NICE in EVs of the triple negative breast cancer cell line MDA-MB-231 and in four sublines that were artificially selected for their metastasis to brain (831), bone (1833), liver (6133) and lung (4175) and are each organotropic for that organ. EV subpopulation signal $I'_{\text{Capture}}^{\Omega}$ (Fig. 6A), $\text{GRE}^{\text{Detection}}$ (Fig. 6B), pairwise $\text{RCE}_{\text{Capture}}^{\text{Detection}}$ (Fig. 6C), and $\text{cNICE}_{\text{Capture}}^{\text{Detection}}$ (Fig. 6D) with tetraspanins (CD81, CD63, and CD9) as well as cancer-associated proteins (CD44 and EGFR) were measured. While the abundance of each antibody-captured subpopulation varied greatly among the sublines (Fig. 6A), their $\text{GRE}^{\text{Detection}}$ scores for all detection targets were similar (Fig. 6B), potentially due to the fact that these cell lines are closely related in lineage. Lung-tropic 4175 EVs had the most abundant ITG- $\beta 4$ subpopulation, followed by parental MDA-MB-231 EVs, consistent with previous literature³⁶. Meanwhile, tetraspanin co-enrichment patterns greatly differed in the ITG- $\beta 4^+$ EV subpopulation of each organotropism: ITG- $\beta 4^+$ EVs of lung-tropic cells only positively co-enriched with CD9 ($\text{NICE}_{\beta 4}^{\text{CD}9} = 4.6$), while negatively co-enriched with CD81 ($\text{NICE}_{\beta 4}^{\text{CD}81} = 0.49$), CD63 ($\text{NICE}_{\beta 4}^{\text{CD}63} = 0.41$) and CD44 ($\text{NICE}_{\beta 4}^{\text{CD}44} = 0.23$); ITG- $\beta 4^+$ EVs of bone-tropic and liver-tropic sublines neutrally or positively co-enriched with all detection targets ($0.82 < \text{NICE} < 8.3$); ITG- $\beta 4^+$ EVs of brain-tropic cells negatively co-enriched with all detection targets examined ($0.13 < \text{NICE} < 0.56$). For 4175 EVs, ITG- $\beta 4$'s binding partner ITG- $\alpha 6$ followed the same co-enrichment trends described above for CD81 ($\text{NICE}_{\alpha 6}^{\text{CD}81} = 0.35$) and CD9 ($\text{NICE}_{\alpha 6}^{\text{CD}9} = 3.5$).

Protein co-enrichments of other integrin-expressing EV subpopulations also varied significantly. Integrin-carrying EVs of brain-tropic 831 negatively co-enriched with all three tetraspanins, as well as CD44 and EGFR. ITG- αV and its binding partner ITG- $\beta 5$ have been linked to liver-tropism for triple negative breast cancer.³⁶ The detection target co-enrichment profile of ITG- αV^+ and ITG- $\beta 5^+$ EVs in liver-tropic 6113 cells was similar. Both were positively co-enriched with CD81 ($\text{NICE}_{\alpha V}^{\text{CD}81} = 2.6, \text{NICE}_{\beta 5}^{\text{CD}81} = 3.6$) and CD9 ($\text{NICE}_{\alpha V}^{\text{CD}9} = 1.7, \text{NICE}_{\beta 5}^{\text{CD}9} = 5.5$), negatively co-enriched with CD44 ($\text{NICE}_{\alpha V}^{\text{CD}44} = 0.21, \text{NICE}_{\beta 5}^{\text{CD}44} = 0.42$), and neutrally co-enriched with CD63 and EGFR. Another integrin, ITG- $\beta 1$, was previously found to be expressed in the EV lysate of lung-tropic 4175 and bone-tropic 1833 cells.³⁶ Here, we observed that ITG- $\beta 1^+$ EVs were positively co-enriched with all detection targets, except in brain-tropic 831 cells. Furthermore, we observed strong co-enrichment of ITG- αV and ITG- $\beta 1$ with CD81 ($\text{NICE}_{\alpha V}^{\text{CD}81} =$

25.8, $NICE_{\beta_1}^{CD81} = 11.8$), CD9 ($NICE_{\alpha V}^{CD9} = 80.3$, $NICE_{\beta_1}^{CD9} = 22.9$) and CD44 ($NICE_{\alpha V}^{CD44} = 9.9$, $NICE_{\beta_1}^{CD44} = 4.1$) in bone-tropic 1833 EVs.

NICE scores for each organotropic cell line are shown in Figure 7. The median NICE score of protein pairs in EVs were positive for parental and liver-tropic cells, neutral for bone- and liver-tropic, and negative for brain-tropic (Fig. 7A and B). The majority (80%) of NICE values fell within a range of 0.2 to 11.5 when considering all cell lines. Visually, the distribution is the narrowest for lung-tropic cell line EVs. The median NICE was above 1 for EVs from all cell lines except the brain-tropic cell line. 82% of NICE scores from brain-tropic 831 EVs were below NICE = 1, with a median of 0.33, thus distinguishing brain tropism from the other organotropic cells studied here.

3. Discussion:

Here, we introduce the concept of co-enrichment of proteins in EVs and mathematically define equations to calculate co-enrichment based on protein concentration. Furthermore, we introduced an analytical framework to assess GRE, RCE, and NICE of proteins in EVs using universal capture and detection probes to sample the overall EV population and provide a measure of EV population and subpopulation density. Using antibody microarrays to measure combinatorial protein co-expression in a high-throughput manner, we calculated and mapped NICE values for multiple proteins in EV populations and found substantial variations across cell lines and protein pairs, covering the range of negative, neutral, and positive co-enrichment. NICE scores of conventional EV markers and cancer-associated proteins in breast cancer EVs revealed differences between parental and organotropic progeny cell lines with different metastatic potential and organotropism, suggesting that NICE could reflect physiological processes and provide information on cell changes and EV biogenesis.

3.1 NICE Methodology and Cross-Validation

The calculation of NICE relies on multiple measurements and parameters. Firstly, the GRE measures the relative expression of a detection protein in an EV population immobilized on a microarray slide using the TIM4 universal capture, normalized with a universal EV dye to adjust for the density of captured EVs. GRE is a population-scale expression measure akin to the one

obtained by MS, ELISA and western blot. For multiple proteins with available literature values, the GRE was concordant with values obtained by MS.^{30,32,36} RCE is computed similarly to the GRE, but the universal capture is replaced by immobilized capture antibodies against a specific target protein. The integrity of immobilized EVs and the expectation that detected proteins could not be found in a protein complex and thus must reside within an individual EVs underpins the ability to derive GRE and RCE from ensemble measurements of EV populations.

3.2 NICE Profiles are Independent of GRE Profiles

While GRE provided useful insight of populational expression level of EVs derived from a given cell line, the co-enrichment pattern within the EV population follows different patterns. GRE^{CD63} varied among BT549, T-47D and MCF-7 EVs (Fig. 5B), where T-47D EVs' GRE^{CD63} was two-fold lower than that of BT549 and MCF-7. However, NICE^{CD63}_{Capture} was neutral or positive for all EV subpopulations examined in all three cell lines. Meanwhile, GRE scores for all detection targets were found to be similar among EVs of the MDA-MB-231 parental and organotropic sublines (Fig. 6B), while the corresponding NICE scores heatmaps fluctuate for all detection targets examined.

3.3 Current and Alternative Choices for Universal Labels for NICE

In addition to cell tracker dyes CFDA-SE and CTR, other universal detection candidates may also be used with minimal changes to the NICE workflow. Endogenous EV labeling via membrane-localizing fluorescent proteins and tagged EV-associated tetraspanins have been presented as an attractive method to fluorescently label EVs without the use of dyes or antibodies. Genetically fusing EV-associated tetraspanins (such as CD63 and CD9) with fluorescent proteins has been a common strategy to enable EV tagging and imaging.^{23,37-41} However, both our data and recent literature have observed vast proteomic heterogeneity found between EV subpopulations identified by different tetraspanins³³⁻³⁵. Thus, we do not believe that fluorescently labelled tetraspanins would be suitable universal detection candidates. Membrane-localizing sequences, such as the murine GAP43 palmitoylation sequence, have also been used to fluorescently label the cell and EV membrane.⁴² While it is known that palmitate has an insertion preference for lipid raft domains

over bulk plasma membranes,^{43,44} it remains unclear how this preference would impose any potential bias in its ability to tag EVs universally.

In our work, we benchmarked and validated phosphatidylserine-binding TIM4 as a suitable universal capture agent for EVs. The performance of TIM4 as an EV isolation agent was recently compared to other isolation methods, such as size-exclusion IZON columns used in our study.⁴⁵ MS data confirmed that the proteomic profile of EVs isolated by TIM4 and size exclusion chromatography columns were broadly similar as indicated by hierarchical clustering. However, while phosphatidylserine is often over-expressed and exposed on the outer leaflet of the plasma membrane in cancer cells, under normal physiological state, the majority of phosphatidylserine is embedded in the inner leaflet and thus inaccessible to potential TIM4 binding.^{46,47} One would expect the efficiency of TIM4 capture to be reduced, which will need to be examined. Alternatives such as peptide ligands that selectively bind to highly curved membranes could also serve as universal capture.⁴⁸ Biotinylation of EVs is another option that may serve either for universal capture or universal detection, but with a number of drawbacks including chemical modification of proteins that may affect antibody binding, and preclusion of the use of biotin for other applications such as for the signal visualization of detection antibodies.

3.4 NICE is Susceptible to Methodological Bias

NICE was established using a custom antibody microarray platform, but it is expected that it will be readily adaptable to other assay formats. The accuracy and precision of NICE are subject to the processes and technologies used to run the assays and make the measurements. The microarray fabrication process,¹⁷ the binding efficiency of the capture and detection antibodies, spatial bias across the microarray slide,⁴⁹ the brightness of the conjugated fluorophore, as well as the sensitivity and linearity of the microarray scanner could all influence NICE. In the case of negative co-enrichment, the detection signal and associated SNR will be lower, and thus NICE is expected to be less accurate. Moreover, low expression and negative co-enrichment could lead to undetectable signals for a co-expressed target protein.

3.5 Multiplexed NICE Measurements Provide Internal Calibration for Undetectable Targets

Multiplexed measurements of co-expression provide inbuilt, contextual information on protein expression within an EV subpopulation, notably in cases where there is no detected co-expression signal of a protein. For instance, consider a population of EVs immobilized via an antibody against protein B. If following incubation with detection antibodies, some co-expressed proteins can be detected, then the absence of signal for protein A (and other proteins) implies lower co-expression, either because of lower GRE, or as a consequence of negative co-enrichment. We can thus foresee scenarios where negative co-enrichment may be undetectable while positive co-enrichment will be detectable, signifying that NICE will be biased towards positive co-enrichment. By triangulating the GRE^A, the fluorescence intensity (detected by the universal fluorescent label) of the subpopulation of EVs expressing protein B, and other detectable co-expressed proteins, one may be able to identify cases where negative co-enrichment is the reason for the absence of signal. Taking into consideration these parameters, it may be possible to predict the detectable negative co-enrichment threshold for a particular protein, and thus determine that a protein is negatively co-enriched beyond this threshold.

3.6 Observed NICE Values Range from Negative to Neutral to Positive

We found that among all the organotropic EV NICE scores, 40.4% of values were positive, 33.3% of values were neutral, while 26.3% were negative (Fig. 7). Although we considered establishing a statistically informed co-enrichment threshold (as opposed to the arbitrary threshold $0.5 < \text{NICE} < 2$) to distinguish between negative, neutral and positive, we refrained from doing so because values would fluctuate across protein pairs and experiments, and because of the experimental intrinsic bias for positive co-enrichment values. Other threshold choices, such as a co-enrichment threshold of 0.33 to 3 could also constitute an alternative as it would encompass one order of magnitude fold change, and future studies may guide the optimal definition of what constitute a neutral NICE vs a positive or negative NICE. Furthermore, while 80% of organotropic NICE values fell between 0.2 to 11.5, NICE for the organotropic EVs ranged from 0.037 to 80.4. 10% of NICE scores (i.e., 25 out of 255) were above 11.5, and specifically 17.6% for EVs from parental cells, 13.7% for liver-tropic cells, 4% for brain- and 2% for lung-tropic cells. The maximum NICE score measured was $\text{NICE}_{\alpha V}^{\text{CD9}} = 80.4$ in bone-tropic 1833 EVs. CD9 and ITG- αV have been shown to associate as a protein complex in endothelial cells to promote angiogenesis⁵⁰,

an essential component of bone metastasis. Such extreme positive co-enrichment pattern was also seen in ITG- αV 's binding partner ITG- $\beta 1$ within EVs of bone-tropic cells. As integrin $\alpha V\beta 1$ has been observed on the membrane of osteoclasts,⁵¹ resident bone cells responsible for bone remodeling and degradation^{52,53}, the extreme positive co-enrichment values are consistent with co-packaging of both proteins into EVs and of $\alpha V^+ \beta 1^+$ EVs playing a functional role in pro-tumor remodeling of bone. Conversely, 10% of all NICE score fell below 0.2, with brain-tropic EVs having the most extreme negative co-enrichment values (27% or 14 out of 51 NICE scores measured). The lowest NICE score measured was $NICE_{CD63}^{EGFR} = 0.037$, also found in EVs of bone-tropic cells (Fig. 6D and Fig. 7A).

Cell line-specific trends of co-enrichment were also observed, with brain-tropic EVs being predominately negative (65% of all its NICE values were below 0.5 and 82% were below 1) with a median NICE = 0.33 (Fig. 7). NICE values for non-brain organotropism were more evenly distributed from < 1 to > 1 , and median NICE indicated positive or neutral co-enrichment. Brain metastasis must overcome the blood-brain barrier, which is distinctive from other organ tropism and could account for its distinct EV protein co-enrichment signature. As brain-tropic breast cancer EVs have been shown to pre-condition the brain microenvironment for subsequent tumor invasion,⁵⁴ we speculate that the abovementioned NICE signature may provide clues to understand the functional role of brain-tropic EVs and the mechanism of breast cancer brain metastasis.

3.7 NICE for single EV measurements

In our work, NICE is defined and calculated based on average measurements reflective of protein concentrations. With the rapid emergence of single EV measurements, measurements of protein co-expression in EVs are becoming more common. Single EV measurements however differ in that they commonly record the absence or presence of a target protein to which a digital value of 0 or 1 can be assigned, respectively. Akin to PCR and ELISA, which both have digital equivalents, it should also be possible to compute NICE based on digital measurements within a probabilistic framework. However in either digital PCR or digital ELISA only individual expression is considered, but not co-expression. The derivation of digital NICE will depend on an accurate account of all EVs and protein expression, including small EVs which may be difficult to label with a high yield and could easily be missed. We foresee that high sensitivity microscopy, down to single fluorophore sensitivity will be a prerequisite for deriving digital NICE accurately. A full

derivation and discussion of digital NICE is beyond the scope of this manuscript and will be reported elsewhere.

4. Conclusion

In conclusion, we introduced RCE and NICE of pairwise protein expression in EVs, a nomenclature and mathematical description of $\text{NICE}_{\text{B}}^{\text{A}}$, and mapped the pairwise concentration-normalized protein co-enrichment (i.e. NICE) of up to 104 combinations per experiment. NICE is normalized using the predicted co-expression under stochastic packaging, while universal labels and capture agents are used to establish the GRE, and compute normalized positive and negative co-enrichment; high SNR of the measured fluorescence signal lends support to the accuracy of NICE scores. NICE supplements conventional protein quantification in lysed EVs (which can be obtained via MS and ELISA, and is equivalent to GRE) and protein-co-expression analysis.

The majority of NICE scores fall within one order of magnitude of $\text{NICE} = 1$, while extreme positive and negative co-enrichment values of 80.4 and 0.037 were recorded. NICE was found to be specific to each protein pair and each cell line, and distinctive NICE patterns emerged for different cell lines, including among parental and organotropic progeny derived from the same cell line. These results indicate that pairwise protein co-enrichment is common, variable, and can reach high values, both for positive and negative co-enrichment. Indeed, whereas between some organotropic cell lines the GRE of the targeted proteins was conserved in EVs, NICE was variable. We can thus surmise that co-enrichment reflects biomolecular changes in the cell and in the biogenesis of EVs, and could serve as a read-out, and possibly a biomarker, for the cell genotype and phenotype.

Single EV protein analysis methods and new methods that have multiplexed analysis capability are predisposed to extend pair-wise NICE to full combinatorial multiplex analysis (i.e. co-enrichment analysis of three or more proteins) but will need to consider the digital nature of those measurements and consider a digital NICE that complements the concentration-based NICE introduced here. NICE analysis requires to establish the total population of EVs, which for ensemble measurements is the GRE, and which requires a universal capture probe and quantification of immobilized EVs detected either using label-free methods, or with a universal label; even if labelling is imperfect, as long as the same method is used for RCE, and the bias is preserved across subpopulations, normalization will yield accurate NICE.

We note that NICE analysis could be extended to include nucleic acids and other molecular cargo contained within EVs, and conducted across different types of molecular cargo, e.g., the co-enrichment of an RNA cargo A in EV subpopulations expressing protein B. We hope that NICE can be used as a new metric to study EV phenotypes, and that it will spur efforts to uncover the mechanisms that govern co-enrichment, and that in turn they will help advance our understanding of the role of biomolecule co-enrichment in EVs in health and disease, its implication for therapy and its potential as a biomarker.

5. Materials and Methods:

Cell Culture

Human colorectal cancer cell line HT29 (ATCC® HTB-38), human breast cancer cell line T47-D, MCF-7, BT549, MDA-MB-231 and its organotropic sublines 1833, 4175, 6113, and 831 were cultured in Dulbecco's Modified Eagle Medium (Gibco, USA) containing 4.5 g/L D-glucose, 4.5 g/L L-glutamine, and 110 mg/mL sodium pyruvate. The media was further supplemented with 10% FBS and 1% penicillin-streptomycin (Gibco, USA). All cell lines were incubated at 37° C with 5% CO₂ supplementation. MDA-MB-231 and its sublines were kindly provided by Professor Peter Siegel of the Goodman Cancer Institute at McGill University.

EV Isolation

Upon the cell lines reaching 50% confluency, cell culture media was replaced with DMEM media containing 5% EV-depleted FBS and collected after 48 hours. The media was centrifuged at 400 x g for 15 minutes, syringe-filtered using a 0.22 um PES membrane filter (Millipore Sigma, USA), and then concentrated using an Amicon Ultra 100kDa NMWCO centrifugal filter unit (Millipore Sigma, USA). The media was concentrated down to 500 µL per every 45 mL raw supernatant and purified using 70 nm qEVoriginal Columns (IZON, USA). Fraction 7 to fraction 10 were pooled for further experiments. Depending on its concentration, the purified EV solution may be further concentrated using a PierceTM PES 100 MWCO 0.5 mL Protein Concentrators (ThermoFisher Scientific, USA).

EV Size and Concentration Characterization

EV particle concentration was accessed by Nanoparticle Tracking Analysis (NTA, NanoSight NS300, Malvern Panalytical, UK) and qNano Turnable Resistive Pulse Sensing instrument (TRPS) (IZON, USA). Depending on its concentration, the purified EV solution may be further concentrated using a PierceTM PES 100 MWCO 0.5 mL Protein Concentrators (Thermofisher Scientific, USA). For NTA, EV samples were diluted in PBS to achieve a concentration of 10^8 - 10^9 particles/mL and loaded to a syringe pump connected to the flow cell chamber. 3 measurements were taken and averaged to calculate the particle concentration. For TRPS, EV samples were diluted in electrolyte buffer and the instrument was primed according to manufacturer's instruction. Samples were loaded onto the top fluid cell and the signal was recorded consecutively for a maximum of 10 minutes. Silica nanoparticles at 100 nm and/or 150 nm were diluted according to manufacturer's instruction and ran before and after the sample measurement, where their signal was used to calculate the final particle size and concentration of EV sample.

Transmission Electron Microscopy

Transmission Electron Microscopy was performed with a FEI Tecnai 12 at a working voltage of 120 kV. EVs samples were store at 4 degrees Celsius before visualisation. Copper grids were negatively charged for 20 sec at 20 mA. A sample of 5 μ L was directly loaded on the grid and incubated for 5 min. Excess was wiped off. Three washing steps were performed in water for 1.5min each. Staining was performed with a 1% uranyl acetate solution for 45 sec. Assistance was provided by Jennie Mui and Kelly Sears at the Facility for Electron Microscope Research (FEMR) unit of McGill University.

Fluorescent EV Labeling with CFDA-SE and Cell Tracker Red

Carboxyfluorescein diacetate succinimidyl ester (CFDA-SE, Thermofisher Scientific, USA) was added to purified EV solution at a concentration of 40 μ M and incubated for 2 hours at 37C. Cell Tracker Red (Thermofisher Scientific, USA) was added to purified EV solution at a concentration of 40 μ M and incubated for 2 hours at room temperature. Access dye was removed using PierceTM PES 100 MWCO 0.5 mL Protein Concentrators.

EV Biotinylation

EZ-Link NHS-LC-LC-Biotin (Thermo Scientific, USA) was added to purified EV solution to achieve a final biotin concentration of 1 mg/mL and incubated at room temperature for 30 minutes. Pierce™ PES 100 MWCO 0.5 mL Protein Concentrators was used to remove unreacted biotin reagent.

Antibody Microarray Fabrication

Antibodies were diluted in spotting buffer containing 15% 2,3-butanediol and 1 M betaine in PBS to achieve a final concentration of 100 µg/mL. TIM4 and streptavidin were diluted in the abovementioned buffer to a final concentration of 300 µg/mL. The solutions were loaded into an Axygen 384-well polypropylene skirted polymerase chain reaction microplate (Fisher Scientific, USA) and the antibody microarray was fabricated onto 2D-Aldehyde glass slides (PolyAn, Germany) using a sciFLEXARRAYER SX (Scienion, Germany) equipped with a single piezo dispense capillary nozzle with coating 1 (Scienion, Germany). A relative humidity of 65% were maintained throughout the fabrication process and the printed microarrays were incubated overnight in the dark in a 70% humidity bell jar.

Antibody Microarray Workflow

The antibody microarray slides were washed in PBS with 0.1% Tween-20 (0.1% PBST) on a rotary shaker at 450 RMP for 15 minutes and then blocked with 0.1% PBST supplemented with 3% BSA for 2 hours at room temperature. After blocking, the slides are dried using a centrifugal slide dryer (Arrayit, USA) and assembled with a 16-well (or 64-well) microarray hybridization chamber (GRACE BIO-LAB, USA). 50 µL purified EV samples (25 µL for 64-well) were loaded to the designated wells and incubated at room temperature 2 hours, then incubated overnight at 4°C. After sample incubation, the wells are washed with PBS for 3 times on shaker and detection antibody were loaded at a concentration between 1 µg ~ 5 µg/mL, diluted in 0.03%PBST with 3%BSA. The slides are incubated at room temperature on shaker for 2 hours. The detection antibody maybe detected using either anti-specie fluorescently labelled secondary antibody or fluorescently labelled streptavidin, at a final concentration of 1 µg/mL diluted in 0.03%PBST with 3%BSA. The wells are washed with PBS for 3 times on shaker and the secondary antibody or streptavidin are loaded and incubated for 1 hour at room temperature on the shaker. Finally, the slides are detached

from the hybridization chamber and washed in a 0.03% PBST bath for 15 minutes on the shaker. The slides are dried using a centrifugal slide dryer and now ready for imaging.

Data Visualization and Analysis

A microarray scanner (InnoScan 1100 AL, Innopsys, France) was used to visualize the microarray slides, where the gain and laser power were adjusted accordingly. ArroyPro 4.5 (Meyer Instruments, USA) was used to quantify the median relative fluorescence unit (RFU) value for each microarray spots. Additionally, the local background was measured by sampling and averaging the median RFU of four corners surrounding the microarray spots. The net RFU was calculated by subtracting the mean RFU of the microarray spot with the generated local background RFU. The extracted data was plotted using Python and Microsoft Excel. NICE scores generated from capture and detection of the same protein target were excluded from analysis. Signal-to-noise-ratio (SNR) of each RFU was computed by dividing signal RFU with the standard deviation of the local background, and plotted linearly as size of individual heatmap cell, with the minimum size indicating a SNR value of 0.5 or less and the maximum size indicating a SNR value of 5 or more.

1. References

1. Kalluri, R. & LeBleu, V. S. The biology, function, and biomedical applications of exosomes. *Science* vol. 367 (2020).
2. Alipoor, S. D. *et al.* The Potential Biomarkers and Immunological Effects of Tumor-Derived Exosomes in Lung Cancer. *Front. Immunol.* **9**, 819 (2018).
3. Maia, J., Caja, S., Strano Moraes, M. C., Couto, N. & Costa-Silva, B. Exosome-based cell-cell communication in the tumor microenvironment. *Frontiers in Cell and Developmental Biology* vol. 6 18 (2018).
4. Van Niel, G., D'Angelo, G. & Raposo, G. Shedding light on the cell biology of extracellular vesicles. *Nature Reviews Molecular Cell Biology* vol. 19 213–228 (2018).
5. Mathieu, M., Martin-Jaular, L., Lavieu, G. & Théry, C. Specificities of secretion and uptake of exosomes and other extracellular vesicles for cell-to-cell communication. *Nature Cell Biology* vol. 21 9–17 (2019).
6. Dagogo-Jack, I. & Shaw, A. T. Tumour heterogeneity and resistance to cancer therapies. *Nature Reviews Clinical Oncology* vol. 15 81–94 (2018).

7. Cui, S., Cheng, Z., Qin, W. & Jiang, L. Exosomes as a liquid biopsy for lung cancer. *Lung Cancer* **116**, 46–54 (2018).
8. Halvaei, S. *et al.* Exosomes in Cancer Liquid Biopsy: A Focus on Breast Cancer. *Mol. Ther. Nucleic Acids* **10**, 131–141 (2018).
9. Antimisiaris, S. G., Mourtas, S. & Marazioti, A. Exosomes and exosome-inspired vesicles for targeted drug delivery. *Pharmaceutics* vol. 10 (2018).
10. Bunggulawa, E. J. *et al.* Recent advancements in the use of exosomes as drug delivery systems 06 Biological Sciences 0601 Biochemistry and Cell Biology. *Journal of Nanobiotechnology* vol. 16 1–13 (2018).
11. Fabbiano, F. *et al.* RNA packaging into extracellular vesicles: An orchestra of RNA-binding proteins? *Journal of Extracellular Vesicles* vol. 10 (2020).
12. Todkar, K. *et al.* Selective packaging of mitochondrial proteins into extracellular vesicles prevents the release of mitochondrial DAMPs. *Nat. Commun.* **12**, 1–12 (2021).
13. Moreno-Gonzalo, O., Villarroya-Beltri, C. & Sánchez-Madrid, F. Post-translational modifications of exosomal proteins. *Frontiers in Immunology* vol. 5 383 (2014).
14. Anand, S., Samuel, M., Kumar, S. & Mathivanan, S. Ticket to a bubble ride: Cargo sorting into exosomes and extracellular vesicles. *Biochimica et Biophysica Acta - Proteins and Proteomics* vol. 1867 140203 (2019).
15. Rodrigues, M., Richards, N., Ning, B., Lyon, C. J. & Hu, T. Y. Rapid Lipid-Based Approach for Normalization of Quantum-Dot-Detected Biomarker Expression on Extracellular Vesicles in Complex Biological Samples. *Nano Lett.* **19**, 7623–7631 (2019).
16. Wu, D. *et al.* Profiling surface proteins on individual exosomes using a proximity barcoding assay. *Nat. Commun.* **10**, 1–10 (2019).
17. Martel, R., Shen, M. L., DeCorwin-Martin, P., Araujo, L. O. F. de & Juncker, D. Extracellular Vesicle Antibody Microarray for Multiplexed Inner and Outer Protein Analysis. *ACS Sensors* **7**, 3817–3828 (2022).
18. Spitzberg, J. D. *et al.* Multiplexed analysis of EV reveals specific biomarker composition with diagnostic impact. *Nat. Commun.* **14**, 1–12 (2023).
19. Dixon, A. C., Dawson, T. R., Di Vizio, D. & Weaver, A. M. Context-specific regulation of extracellular vesicle biogenesis and cargo selection. *Nat. Rev. Mol. Cell Biol.* 1–23 (2023) doi:10.1038/s41580-023-00576-0.

20. Fidler, I. J., Schroit, A. J., Connor, J., Bucana, C. D. & Fidler, I. J. Elevated Expression of Phosphatidylserine in the Outer Membrane Leaflet of Human Tumor Cells and Recognition by Activated Human Blood Monocytes. *Cancer Res.* **51**, 3062–3066 (1991).
21. Guo, K. *et al.* Calibration-free analysis of surface proteins on single extracellular vesicles enabled by DNA nanostructure. *Biosens. Bioelectron.* **192**, 113502 (2021).
22. Morales-Kastresana, A. *et al.* Labeling extracellular vesicles for nanoscale flow cytometry. *Sci. Rep.* **7**, 1–10 (2017).
23. Chuo, S. T. Y., Chien, J. C. Y. & Lai, C. P. K. Imaging extracellular vesicles: Current and emerging methods. *Journal of Biomedical Science* vol. 25 1–10 (2018).
24. Pužar Dominkuš, P. *et al.* PKH26 labeling of extracellular vesicles: Characterization and cellular internalization of contaminating PKH26 nanoparticles. *Biochim. Biophys. Acta - Biomembr.* **1860**, 1350–1361 (2018).
25. Dehghani, M., Gulvin, S. M., Flax, J. & Gaborski, T. R. Systematic Evaluation of PKH Labelling on Extracellular Vesicle Size by Nanoparticle Tracking Analysis. *Sci. Rep.* **10**, 1–10 (2020).
26. Miyanishi, M. *et al.* Identification of Tim4 as a phosphatidylserine receptor. *Nature* **450**, 435–439 (2007).
27. Nakai, W. *et al.* A novel affinity-based method for the isolation of highly purified extracellular vesicles. *Sci. Rep.* **6**, 1–11 (2016).
28. Ma, Y. *et al.* Identification of small compounds regulating the secretion of extracellular vesicles via a TIM4-affinity ELISA. *Sci. Rep.* **11**, 1–13 (2021).
29. Hamidi, H. & Ivaska, J. Every step of the way: Integrins in cancer progression and metastasis. *Nature Reviews Cancer* vol. 18 533–548 (2018).
30. Dalla, P. V., Santos, J., Milthorpe, B. K. & Padula, M. P. Selectively-packaged proteins in breast cancer extracellular vesicles involved in metastasis. *Int. J. Mol. Sci.* **21**, 1–16 (2020).
31. Bauer, K. R., Brown, M., Cress, R. D., Parise, C. A. & Caggiano, V. Descriptive analysis of estrogen receptor (ER)-negative, progesterone receptor (PR)-negative, and HER2-negative invasive breast cancer, the so-called triple-negative phenotype: A population-based study from the California Cancer Registry. *Cancer* **109**, 1721–1728 (2007).
32. Rontogianni, S. *et al.* Proteomic profiling of extracellular vesicles allows for human breast cancer subtyping. *Commun. Biol.* **2**, (2019).

33. Mizenko, R. R. *et al.* Tetraspanins are unevenly distributed across single extracellular vesicles and bias sensitivity to multiplexed cancer biomarkers. *J. Nanobiotechnology* **19**, 1–17 (2021).
34. Kowal, J. *et al.* Proteomic comparison defines novel markers to characterize heterogeneous populations of extracellular vesicle subtypes. *Proc. Natl. Acad. Sci. U. S. A.* **113**, E968–E977 (2016).
35. Koliha, N. *et al.* A novel multiplex bead-based platform highlights the diversity of extracellular vesicles. *J. Extracell. Vesicles* **5**, (2016).
36. Hoshino, A. *et al.* Tumour exosome integrins determine organotropic metastasis. *Nature* **527**, 329–335 (2015).
37. Mittelbrunn, M. *et al.* Unidirectional transfer of microRNA-loaded exosomes from T cells to antigen-presenting cells. *Nat. Commun.* **2**, (2011).
38. Suetsugu, A. *et al.* Imaging exosome transfer from breast cancer cells to stroma at metastatic sites in orthotopic nude-mouse models. *Advanced Drug Delivery Reviews* vol. 65 383–390 (2013).
39. Piao, Y. J. *et al.* Breast cancer cell-derived exosomes and macrophage polarization are associated with lymph node metastasis. *Oncotarget* **9**, 7398–7410 (2018).
40. Corso, G. *et al.* Systematic characterization of extracellular vesicles sorting domains and quantification at the single molecule–single vesicle level by fluorescence correlation spectroscopy and single particle imaging. *J. Extracell. Vesicles* **8**, (2019).
41. Verweij, F. J. *et al.* The power of imaging to understand extracellular vesicle biology in vivo. *Nature Methods* vol. 18 1013–1026 (2021).
42. Lai, C. P. *et al.* Visualization and tracking of tumour extracellular vesicle delivery and RNA translation using multiplexed reporters. *Nat. Commun.* **6**, (2015).
43. Yang, X., Chatterjee, V., Ma, Y., Zheng, E. & Yuan, S. Y. Protein Palmitoylation in Leukocyte Signaling and Function. *Frontiers in Cell and Developmental Biology* vol. 8 1167 (2020).
44. Resh, M. D. Covalent lipid modifications of proteins. *Current Biology* vol. 23 R431 (2013).
45. Veerman, R. E. *et al.* Molecular evaluation of five different isolation methods for extracellular vesicles reveals different clinical applicability and subcellular origin. *J. Extracell. Vesicles* **10**, e12128 (2021).

46. Szlasa, W., Zendran, I., Zalesińska, A., Tarek, M. & Kulbacka, J. Lipid composition of the cancer cell membrane. *Journal of Bioenergetics and Biomembranes* vol. 52 321–342 (2020).
47. Sharma, B. & Kanwar, S. S. *Phosphatidylserine: A cancer cell targeting biomarker. Seminars in Cancer Biology* vol. 52 17–25 (Academic Press, 2018).
48. Gori, A. *et al.* Membrane-binding peptides for extracellular vesicles on-chip analysis. *J. Extracell. Vesicles* **9**, (2020).
49. Normandeau, F., Ng, A., Beaugrand, M. & Juncker, D. Spatial Bias in Antibody Microarrays May Be an Underappreciated Source of Variability. *ACS Sensors* **6**, 1796–1806 (2021).
50. Peddibhotla, S. S. D. *et al.* Tetraspanin CD9 links junctional adhesion molecule-A to $\alpha\beta 3$ integrin to mediate basic fibroblast growth factor-specific angiogenic signaling. *Mol. Biol. Cell* **24**, 933–944 (2013).
51. Nesbitt, S., Nesbit, A., Helfrich, M. & Horton, M. Biochemical characterization of human osteoclast integrins. Osteoclasts express alpha v beta 3, alpha 2 beta 1, and alpha v beta 1 integrins. *J. Biol. Chem.* **268**, 16737–16745 (1993).
52. Schneider, J. G., Amend, S. R. & Weilbaecher, K. N. Integrins and bone metastasis: Integrating tumor cell and stromal cell interactions. *Bone* vol. 48 54–65 (2011).
53. Duong, L. T., Lakkakorpi, P., Nakamura, I. & Rodan, G. A. Integrins and signaling in osteoclast function. *Matrix Biology* vol. 19 97–105 (2000).
54. Rodrigues, G. *et al.* Tumour exosomal CEMIP protein promotes cancer cell colonization in brain metastasis. *Nat. Cell Biol.* **21**, 1403–1412 (2019).

Mathematical Representation	Interpretation	Explanation and Caveat
I_B^A	fluorescent signal I with A as detection target (revealed using fluorescent anti-A antibodies) for the EV subpopulation enriched based on the expression of B	I is the arbitrary fluorescence intensity obtained from the microarray scanner after background correction.
I_B^{Ω}	fluorescent signal I' with universal EV dye Ω for the EV subpopulation enriched based on the expression of B. Represents the abundance of the captured B ⁺ EV subpopulation.	The fluorescence for EV presence via EV dye may not be proportional to the fluorescence of antibody expression as the dye signal is volumetric.
RCE_B^A	Relative co-expression with B as capture target and A as detection target normalized with universal dye signal	Calculated from $\frac{I_B^A}{I_B^{\Omega}}$
I_{Σ}^A	fluorescent signal generated with 'universal' capture affinity binder Σ and A as fluorescent detection target	
I_{Σ}^{Ω}	Relative fluorescent signal generated with universal capture Σ as capture target and universal detection dye Ω as detection target	
GRE^A	Global relative expression (for A as detection target) with the universal capture binder Σ	$GRE^A = \frac{I_{\Sigma}^A}{I_{\Sigma}^{\Omega}}$
$NICE_B^A$	Normalized index of co-enrichment of A on EVs immobilized via B; NICE = 1 for stochastic inclusion of A in the subpopulation B	$NICE_B^A = \frac{RCE_B^A}{GRE^A}$

Table 1. Definition of parameters underpinning the calculation of NICE inspired from probabilistic terminology, along with their interpretation and explanations.

Normalized Index of Co-Enrichment (NICE)

 protein A

 EV dye

 protein B

 Fluorescent anti-A

 Universal EV capture probe

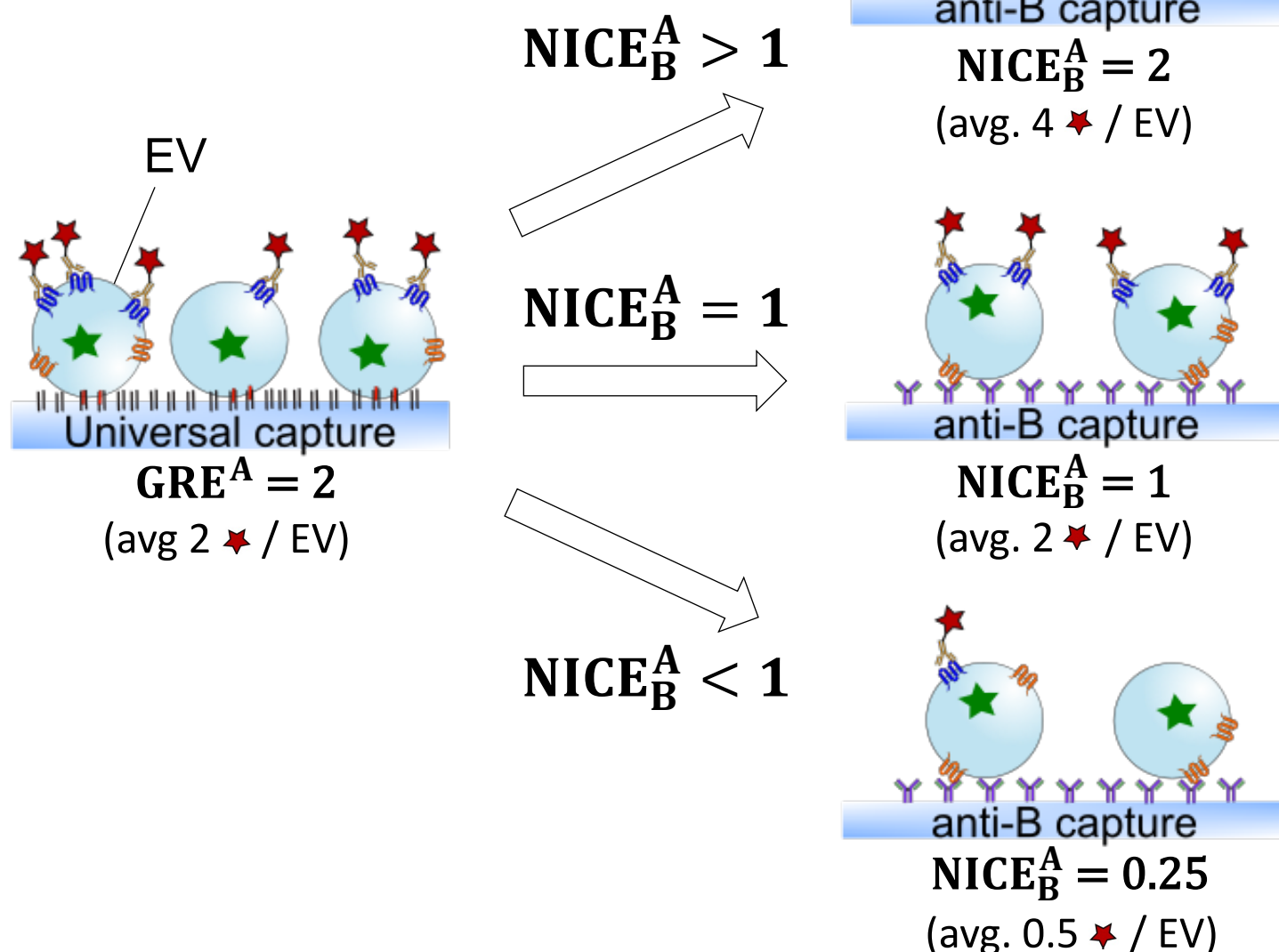


Figure 1. The normalized Index of co-enrichment (NICE) is the ratio of co-enrichment of a protein A and a protein B in individual EVs relative to the predicted co-expression of protein A in EVs expressing B. The predicted co-expression is calculated based on the global relative expression (GRE^A) of protein A in the entire EV population (including EVs that do not express B). GRE^A for protein A was established thanks to two universal probes, one for labelling EVs, and one for capturing them, and fluorescent anti-A detection antibody. $NICE_B^A$ was obtained using the same universal label and anti-A antibody, but using anti-B antibody to capture the subpopulation of EVs that express protein B. $NICE = 1$ when protein A co-expression in the subpopulation of EVs expressing protein B matches the predicted co-expression based on stochastic inclusion of protein A. If the co-expression of protein A is greater or lower than predicted, then $NICE_B^A > 1$ or < 1 , and A is positively or negatively co-enriched with B, respectively. To account for experimental imprecision and natural biological variation, we arbitrarily define thresholds for positive and negative (i.e. depletion) co-enrichment as $NICE > 2$ or < 0.5 , respectively, and neutral co-enrichment as $0.5 \leq NICE \leq 2$.

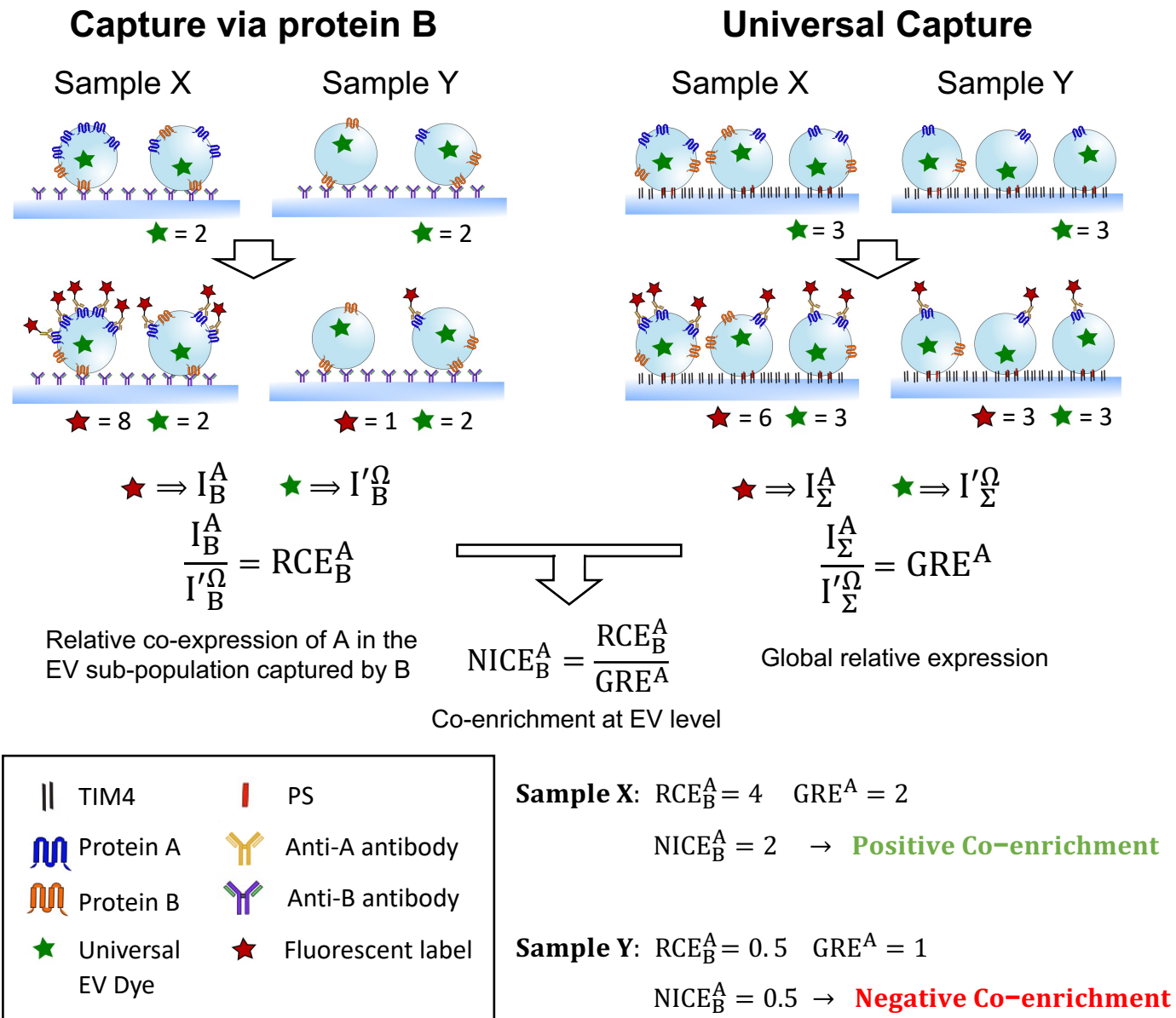


Figure 2. Graphical illustration of NICE calculation and experimental workflow. EVs are captured either via a surface bound universal capture affinity binder Σ (e.g. TIM4 that binds phosphatidylserine) or via anti-protein B antibody that binds EVs expressing protein B at their surface. Next, the expression of protein A on EVs is detected via a fluorescently labelled anti-protein A antibody along with the fluorescence intensity of the universal dye Ω . The relative co-expression of protein A (RCE_B^A) of EVs captured with anti-B antibodies and for EVs captured with Σ (GRE^A) are calculated by normalizing fluorescence of A with fluorescence of Ω . Finally, $NICE_B^A$ is calculated by normalizing RCE_B^A by dividing it by GRE^A , yielding $NICE \approx 1$ if the relative co-expression of A is similar in the B subpopulation than in the entire population, and $NICE \gg 1$ or $\ll 1$ if A is co-enriched with B positively or negatively, respectively.

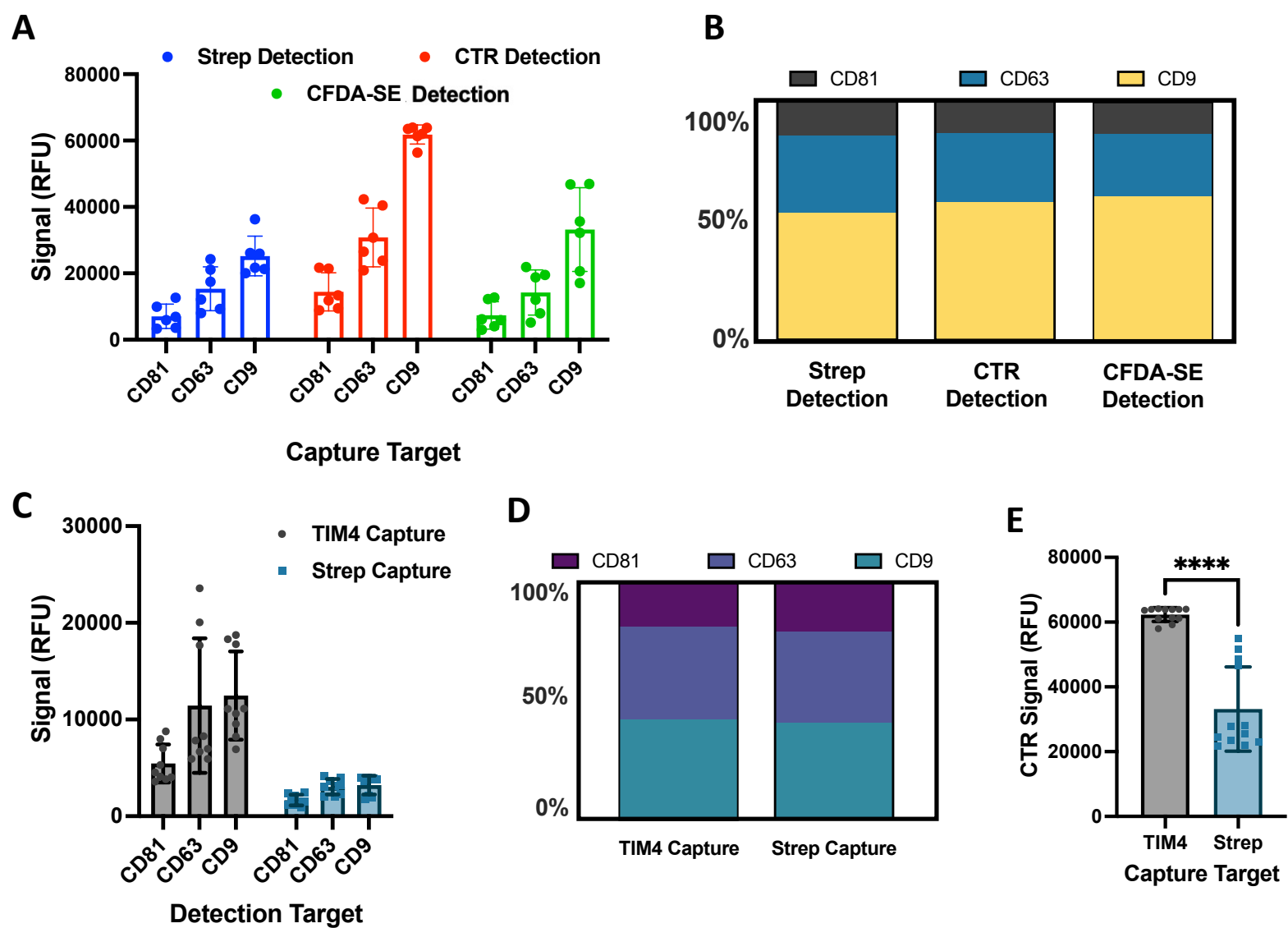


Figure 3. Validation of CFDA-SE and CTR as universal EV labels and TIM4 as universal EV capture. Biotinylated EVs from HT29 cells dyed with either CFDA-SE or CTR were captured on microarrays of anti-CD81, anti-CD63, anti-CD9 antibodies, TIM4, and streptavidin, and subsequently incubated with fluorescent streptavidin or fluorescently conjugated secondary antibodies. **(A)** RFU signal and **(B)** ratio for streptavidin, CTR and CFDA-SE fluorescence for CD81⁺, CD63⁺, CD9⁺ EV subpopulation (defined by the capture antibody). Data shows 3 biological replicates with 10 technical repeats each (biological repeat N = 3, technical repeat n = 10). **(C)** RFU signal and **(D)** ratio of CD81, CD63, and CD9 detected on EVs captured by either TIM4 or streptavidin. **(E)** Total RFU for CD81, CD63, and CD9 detected on EVs captured by either TIM4 or streptavidin (analyzed using one-way ANOVA analysis, **** $p < 0.0001$). Data shows 3 biological replicates with 20 technical repeats each (N = 3, n = 20). Despite the difference in total amount of captured EVs on TIM4 and streptavidin microarrays, the ratio of tetraspanin expression was preserved. Error bars indicate standard deviations between biological replicates.

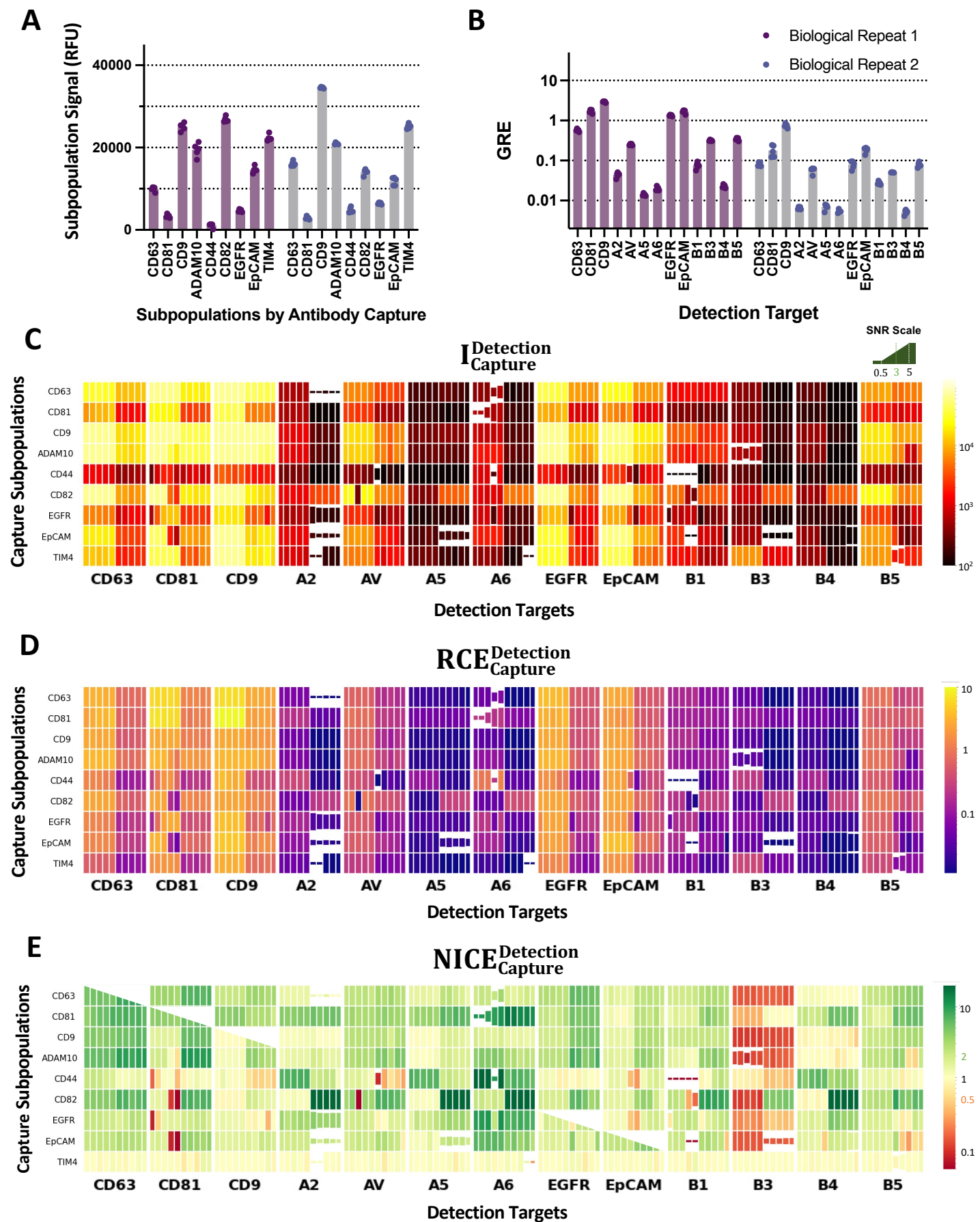


Figure 4. Subpopulation signal, GRE, RCE, and NICE of proteins on EVs from T47D cells labeled with CFDA-SE. A microarray with 8 different capture targets and universal capture TIM4 was incubated with cell-derived EVs and followed by 13 different detection targets and streptavidin. **(A)** Subpopulation signal for each EV subpopulation for two repeats. Error bars indicate standard deviation of 5 technical repeats per each biological repeats ($N = 2$, $n = 5$). **(B)** GRE of the detection targets for EVs captured by TIM4. **(C)** RFU signals for each capture and detection combinations from the microarray image showing individual technical repeats. The SNR value for each individual measurement is reported as the height of the heatmap rectangle increasing from 0.5 – 5; smaller and larger SNR values are shown using the minimal and maximal value, respectively. **(D)** Combinatorial RCE and **(E)** NICE maps showing negative, neutral ($0.5 < \text{NICE} < 2$) and positive co-enrichment. SNRs are the ones calculated in (C). White triangles indicate NICE scores generated from capture and detection of the same protein target and those values were excluded from analysis.

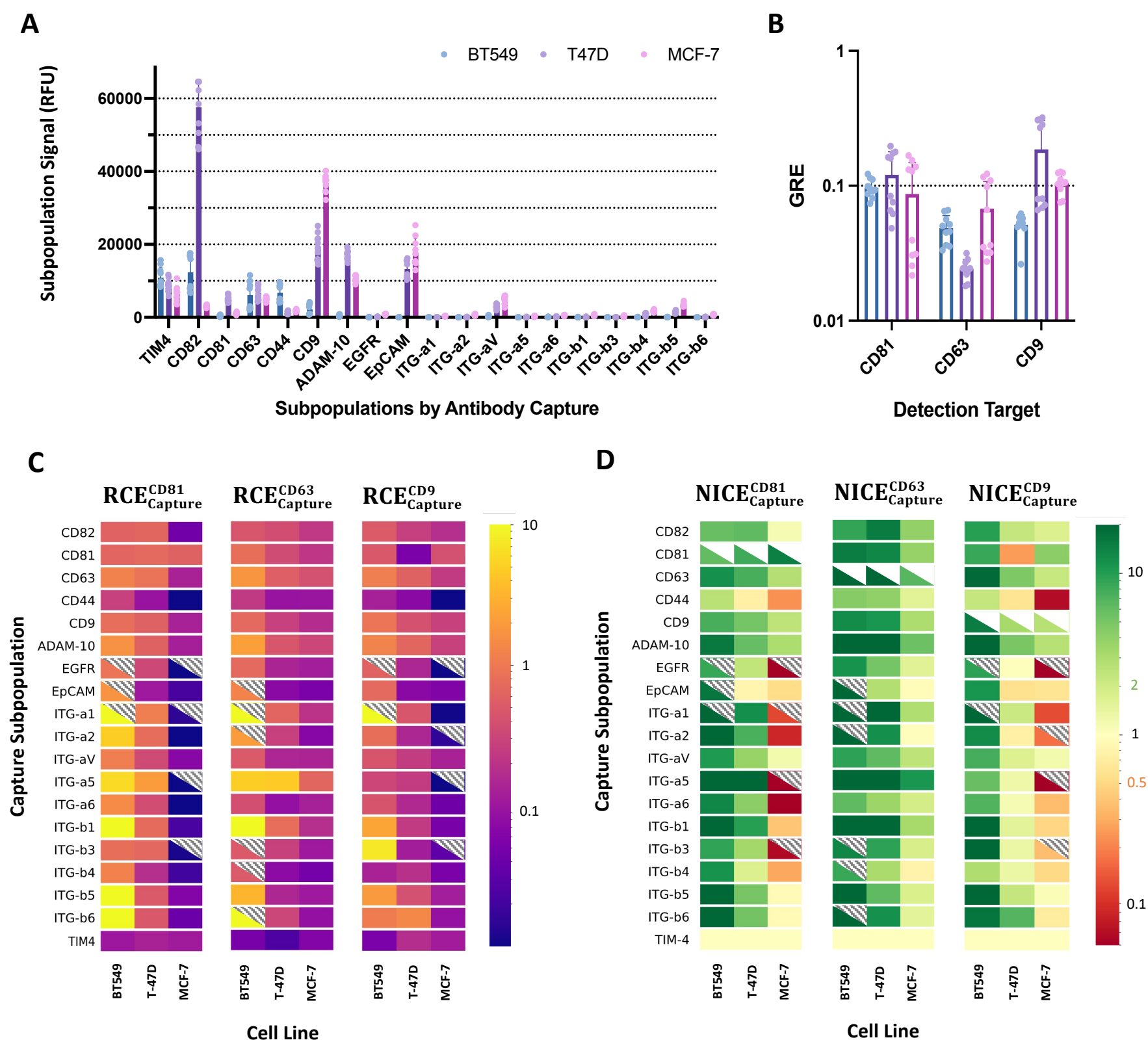


Figure 5. Subpopulation signal, GRE, RCE, and NICE of proteins in EVs derived from 3 breast cancer cell lines with differing metastatic potential. **(A)** Subpopulation signal of each antibody-captured EV subpopulation, where the RFU signal of CTR is used as an estimation of the abundance of the captured EV subpopulations. Each dot represents a single technical repeat, solid bars indicate the mean of the 2 biological repeats (N = 2, n = 5). Error bar indicates the standard deviation of the biological repeats. **(B)** GRE of tetraspanins CD81, CD63, CD9. **(C)** RCE^{CD81}, RCE^{CD63}, RCE^{CD9} and **(D)** NICE^{CD81}, NICE^{CD63}, NICE^{CD9} for EVs derived from breast cancer cell lines of varying metastatic potentials. Heatmap block represents the average of 2 biological repeats with 5 technical repeats each. Hashed triangles for RCE and NICE values indicate SNR < 3 for the majority of the repeats. White triangles indicate NICE scores generated from capture and detection of the same protein target which were excluded from analysis. Tetraspanins CD9, CD63 or CD81 can be either negatively, neutrally, or positively co-enriched depending on cell line and co-expressed protein.

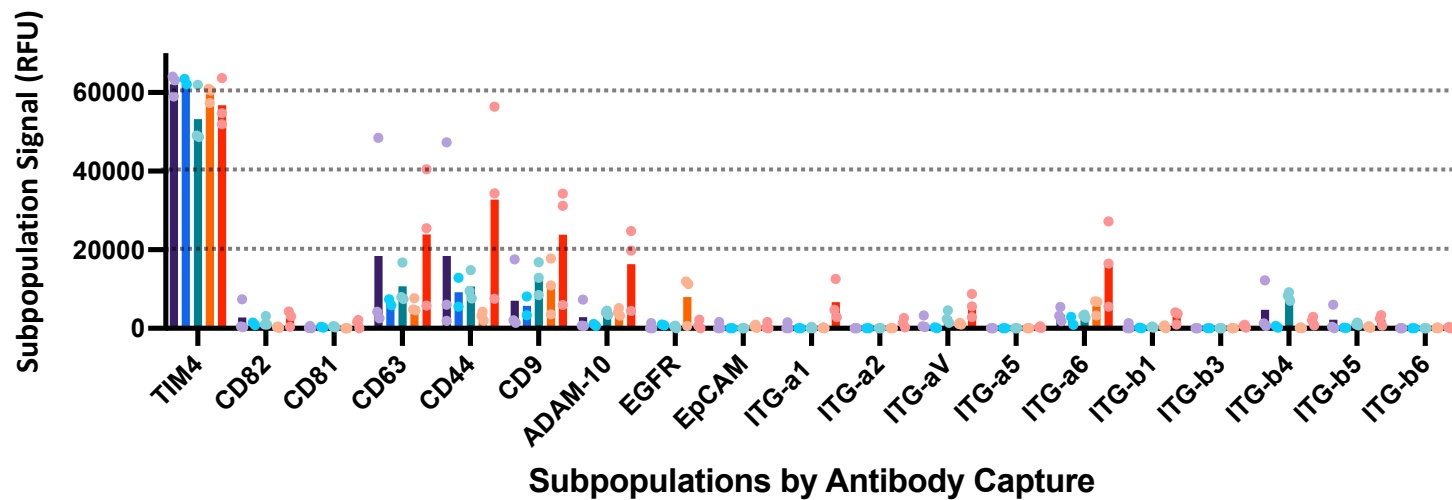
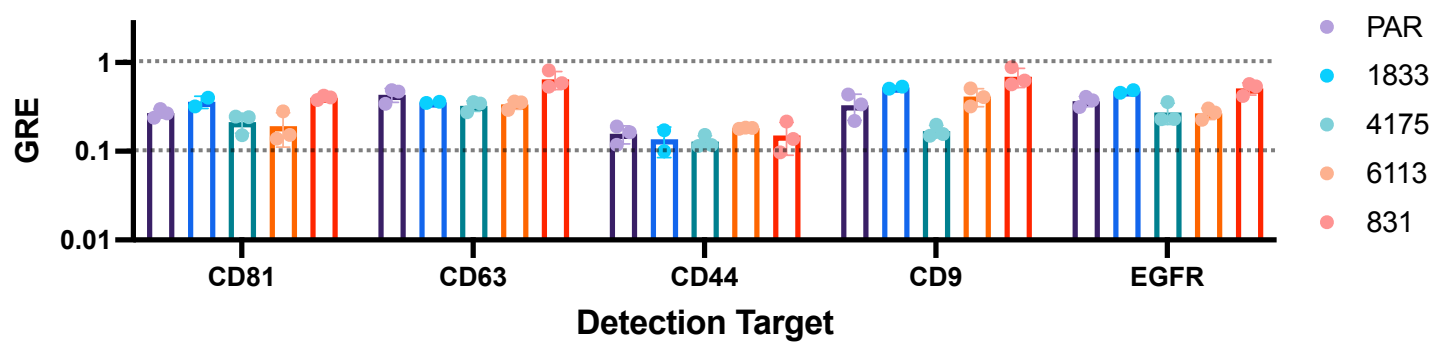
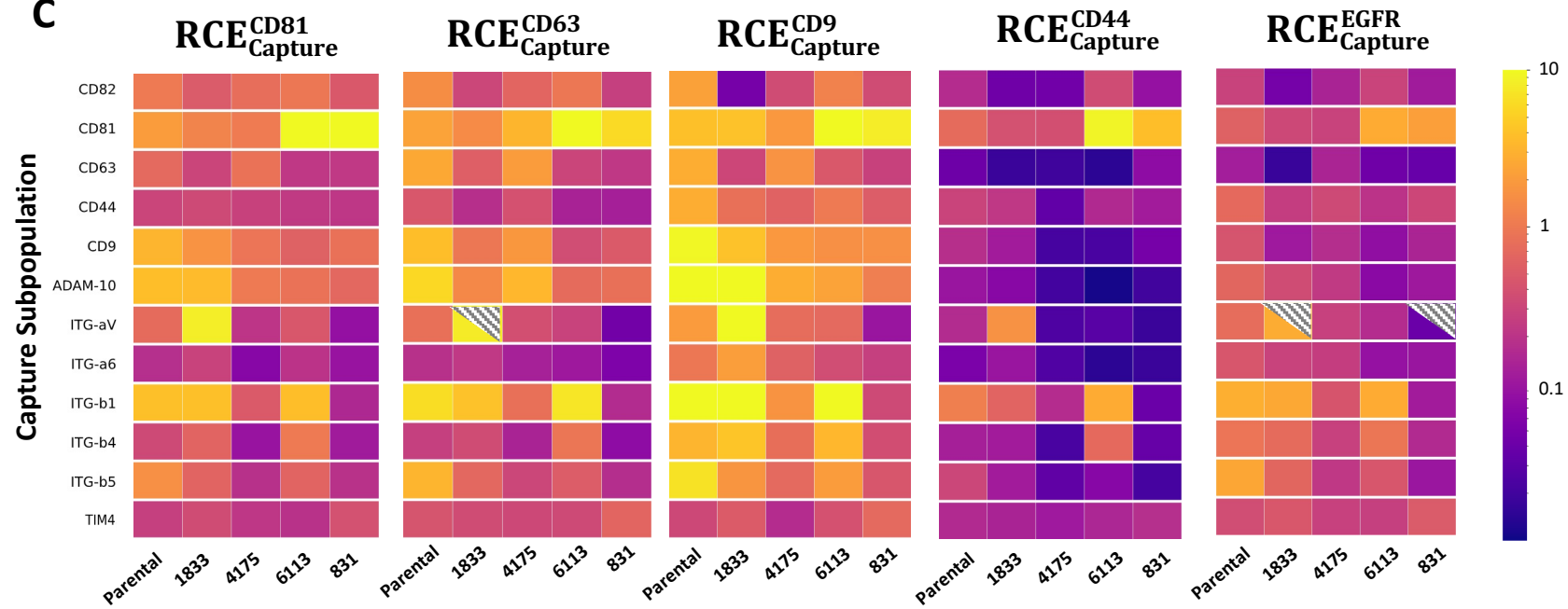
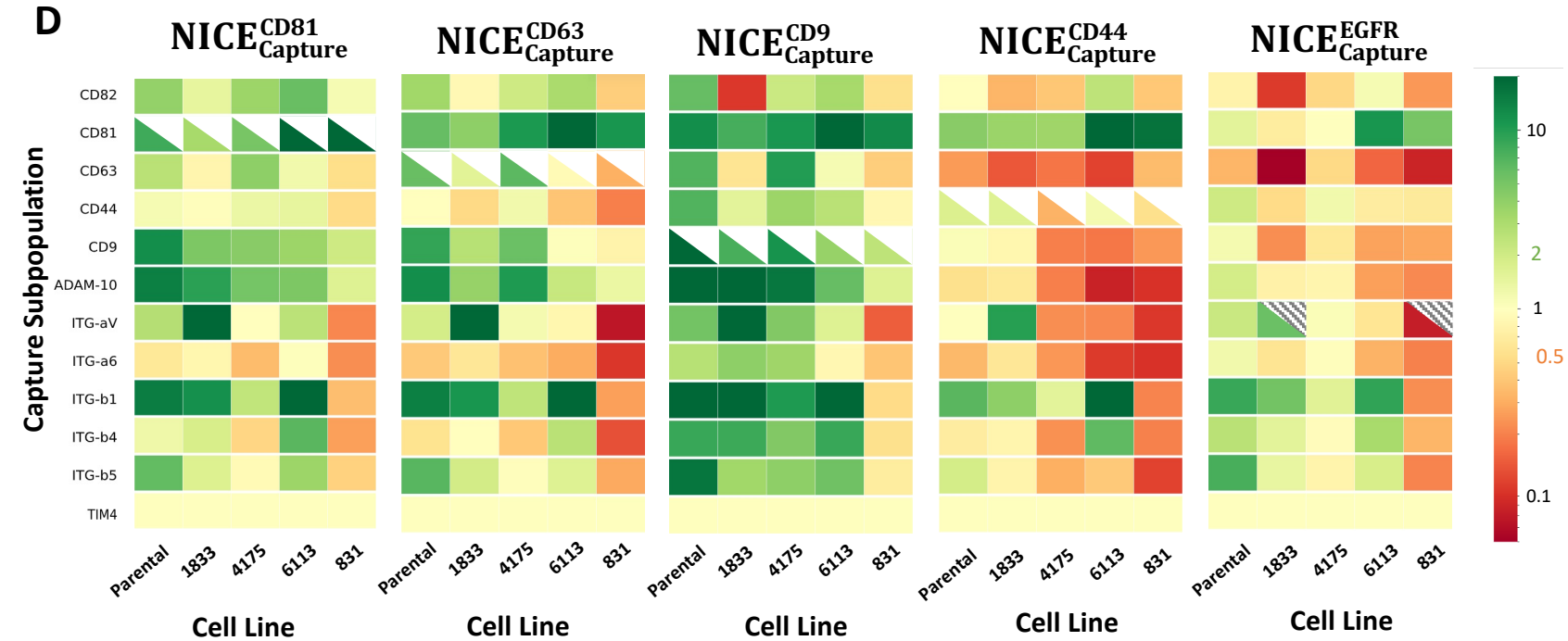
A**B****C****D**

Figure 6. Subpopulation signal, GRE, RCE, and NICE of proteins in EVs derived from triple negative breast cancer cell line MDA-MB-231 (PAR) and its bone- (1833), lung- (4175), liver- (6113) and brain- (831) organotropic sub-lines. **(A)** Subpopulation signal of each antibody-captured EV subpopulations, where the RFU signal of CTR is used as an estimation of the abundance of the captured EV subpopulation. Each dot represents a single technical repeat, solid bars indicate the mean of the 3 biological repeat (N = 3, n = 5). Error bar indicates the standard deviation of the biological repeats. One outlier biological repeat from bone-tropic 1833 was removed due to microarray functionalization abnormality. **(B)** GRE of tetraspanins CD81, CD63, CD9 and cancer associated markers CD44 and EGFR. **(C)** RCE^{CD81} , RCE^{CD63} , RCE^{CD9} , RCE^{CD44} , RCE^{EGFR} and **(D)** $NICE^{CD81}$, $NICE^{CD63}$, $NICE^{CD9}$, $NICE^{CD44}$, $NICE^{EGFR}$ of EVs derived from triple-negative breast cancer cell line MDA-MB-231 and its organotropic sub-lines. Heatmap block represents the average of 3 biological repeats with 5 technical repeats each (N = 3, n = 5). RCE and NICE values greyed out with hashed triangles indicate that more than half of the corresponding 15 repeats had a SNR < 3. White triangles indicate NICE scores generated from capture and detection of the same protein target which were excluded from analysis. The RCE and NICE values of capture targets ITG- α 1, - α 2, - α 5, - β 3, and - β 6 were omitted in the heatmap due to low SNR, but shown in Supplementary Figure S4 and S5. NICE values are generally not correlated to GRE values, e.g. GRE for CD9 and CD44 are similar in cell line 4175, yet NICE values of CD9 are >1, while NICE values for CD44 are broadly < 1.

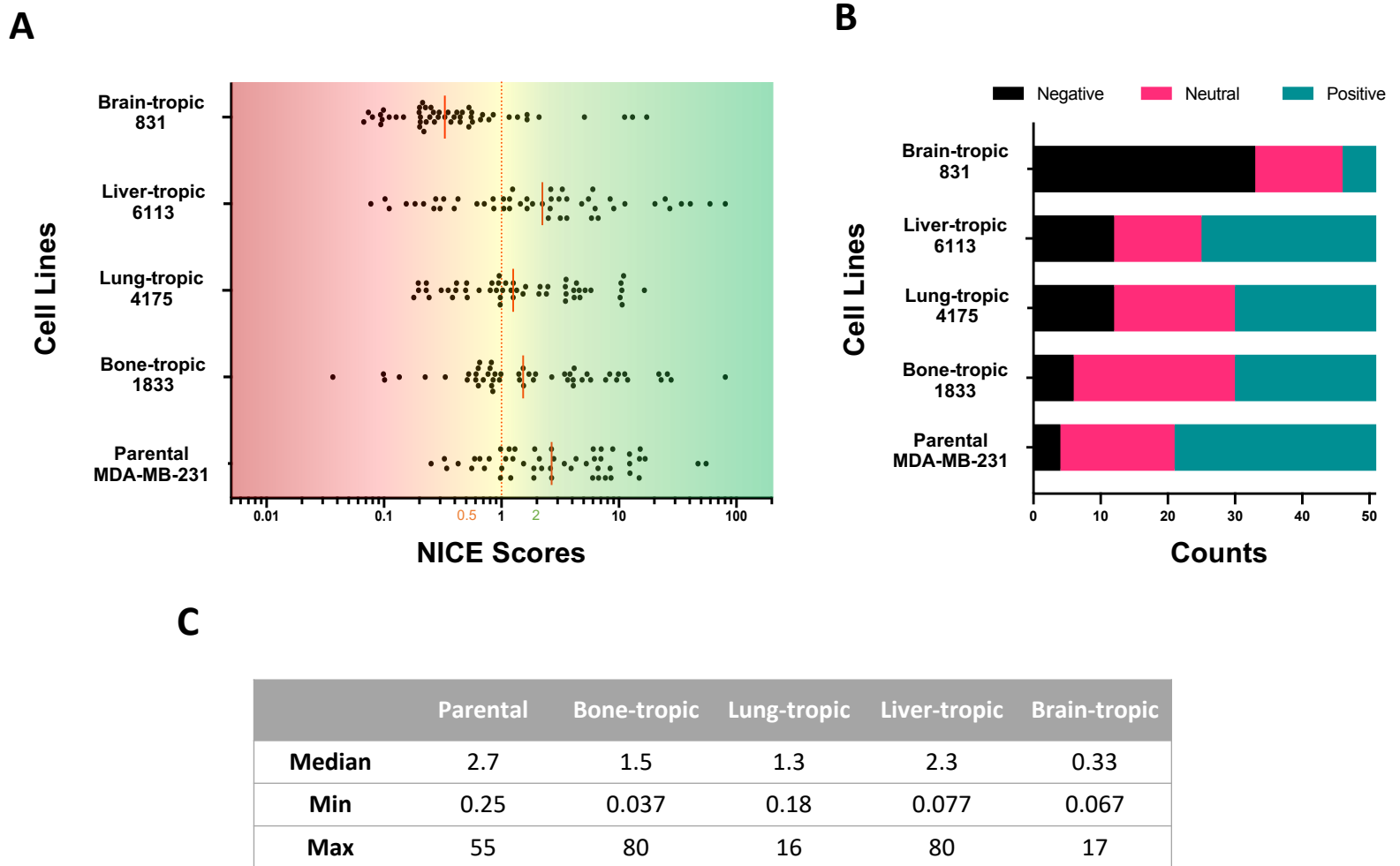


Figure 7. Pairwise NICE scores in EVs derived from triple-negative breast cancer cell line MDA-MB-231 and its bone-, lung- and brain-organotropic sub-lines. **(A)** Scatter plot of 51 NICE scores for each cell line for 11 capture subpopulations (see Fig. 5) and 5 detection targets (CD81, CD63, CD9, CD44, EGFR). NICE scores generated from capture and detection of the same protein target were excluded from analysis. Red line indicates the median. **(B)** Total counts of negative, neutral and positive NICE scores, with neutral being defined as ranging from 0.5 to 2. The size of positive and negative populations is largest for cell lines with negative and positive median values respectively. Interestingly, the parental cell line has the smallest negative population size, while neutral populations size only varies minimally across cell lines. **(C)** Numeric values including extremes for each cell line.

Protein Co-Enrichment Analysis of Extracellular Vesicles

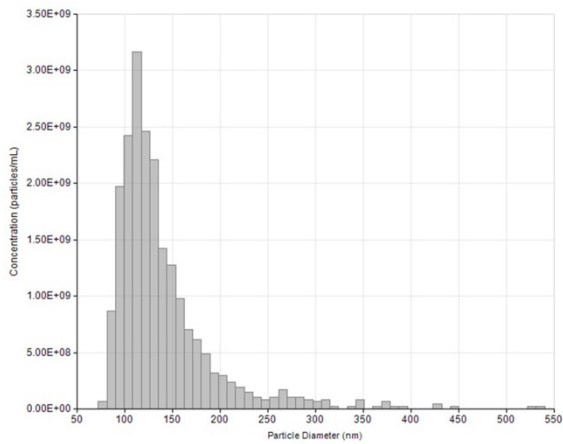
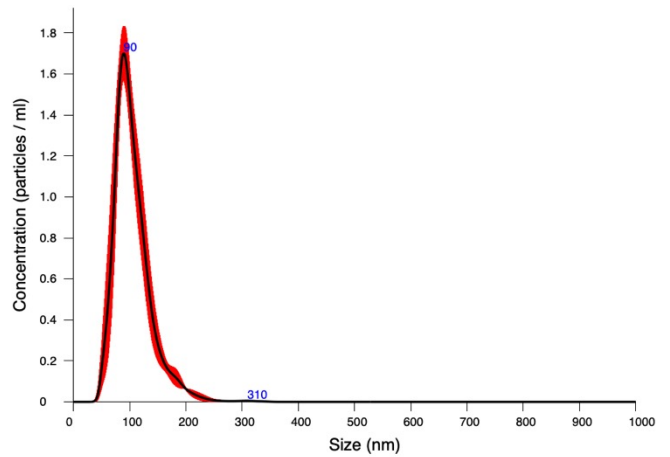
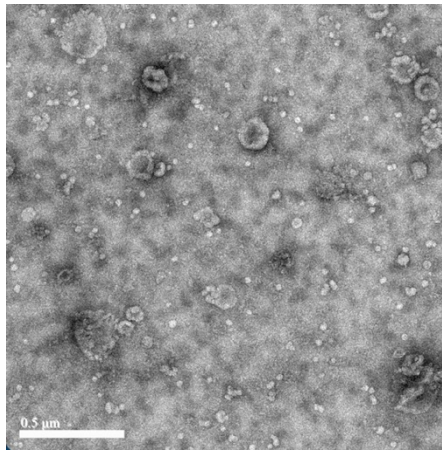
Molly L. Shen^{1,2}, Zijie Jin^{1,2,†}, Rosalie Martel^{1,2,†}, Andreas Wallucks^{1,2}, Lucile Alexandre^{1,2}, Philippe DeCorwin-Martin^{1,2}, Lorena Oliveira Fernandes de Araujo^{1,2}, Andy Ng^{1,2}, David Juncker^{1,2,*}

¹Biomedical Engineering Department, McGill University, Montreal,
QC, Canada

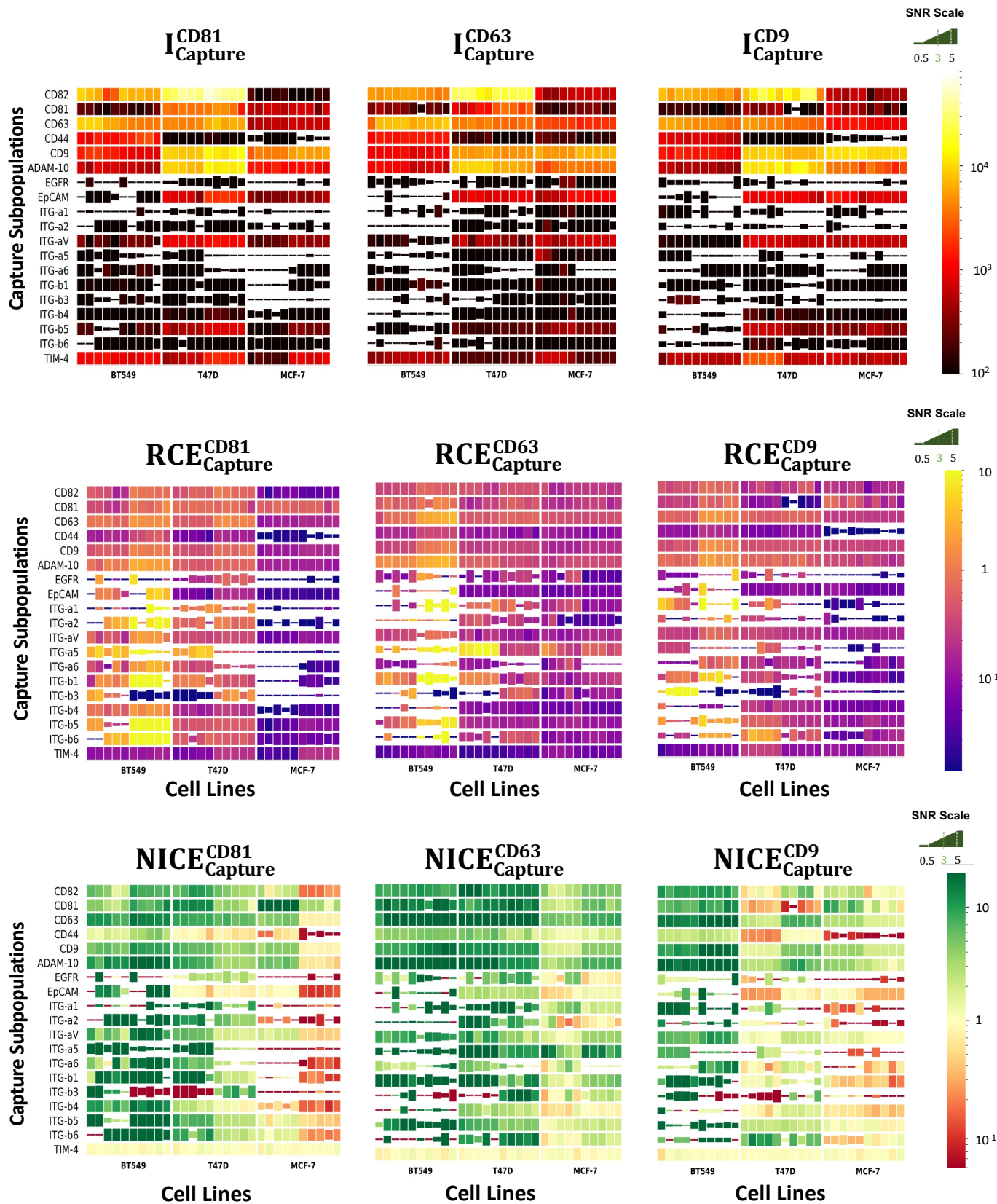
²McGill University & Genome Quebec Innovation Centre, McGill University,
Montreal, QC, Canada

† Z.J. and R.M. contributed equally.

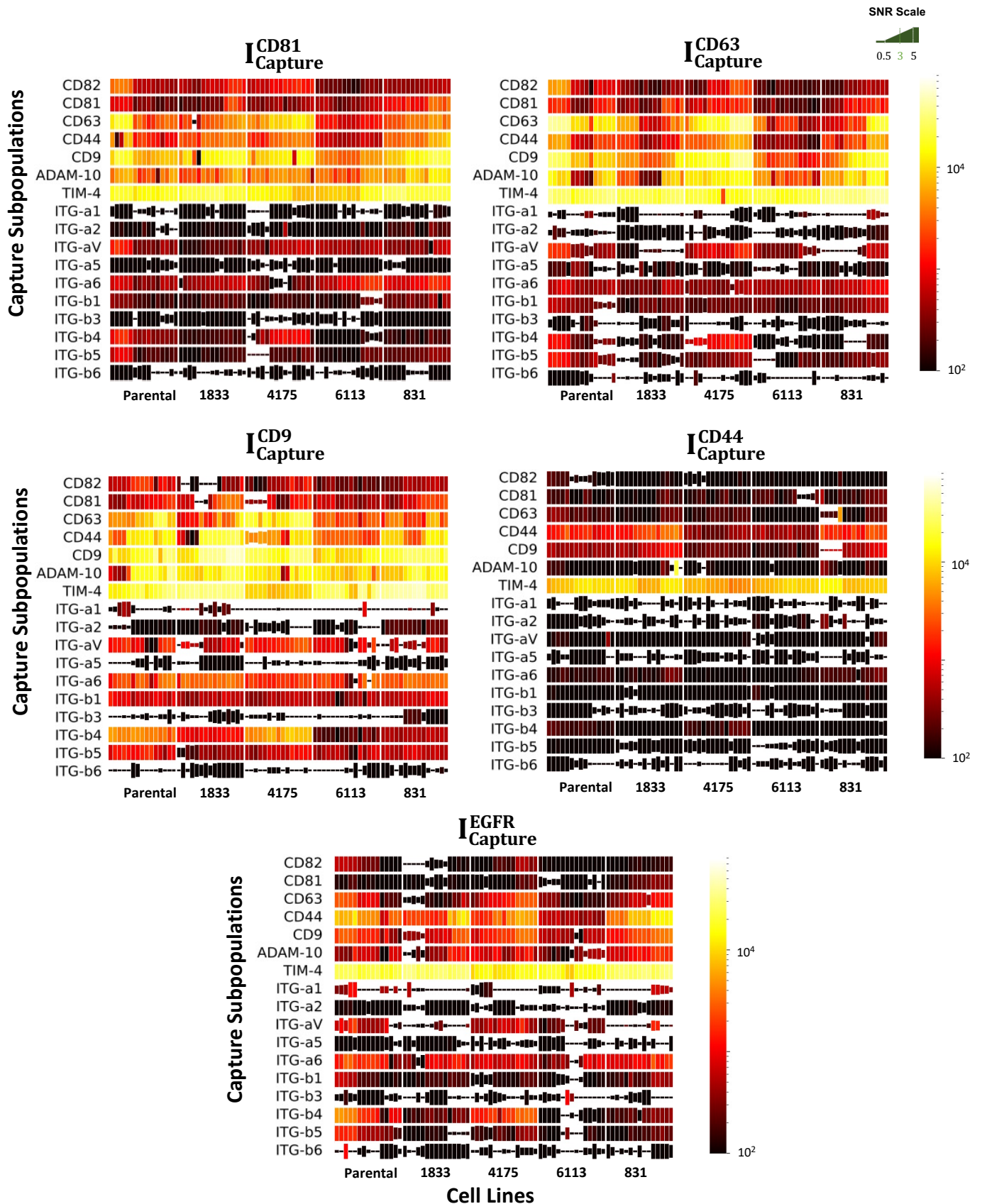
Supplementary Figures

A**B****C**

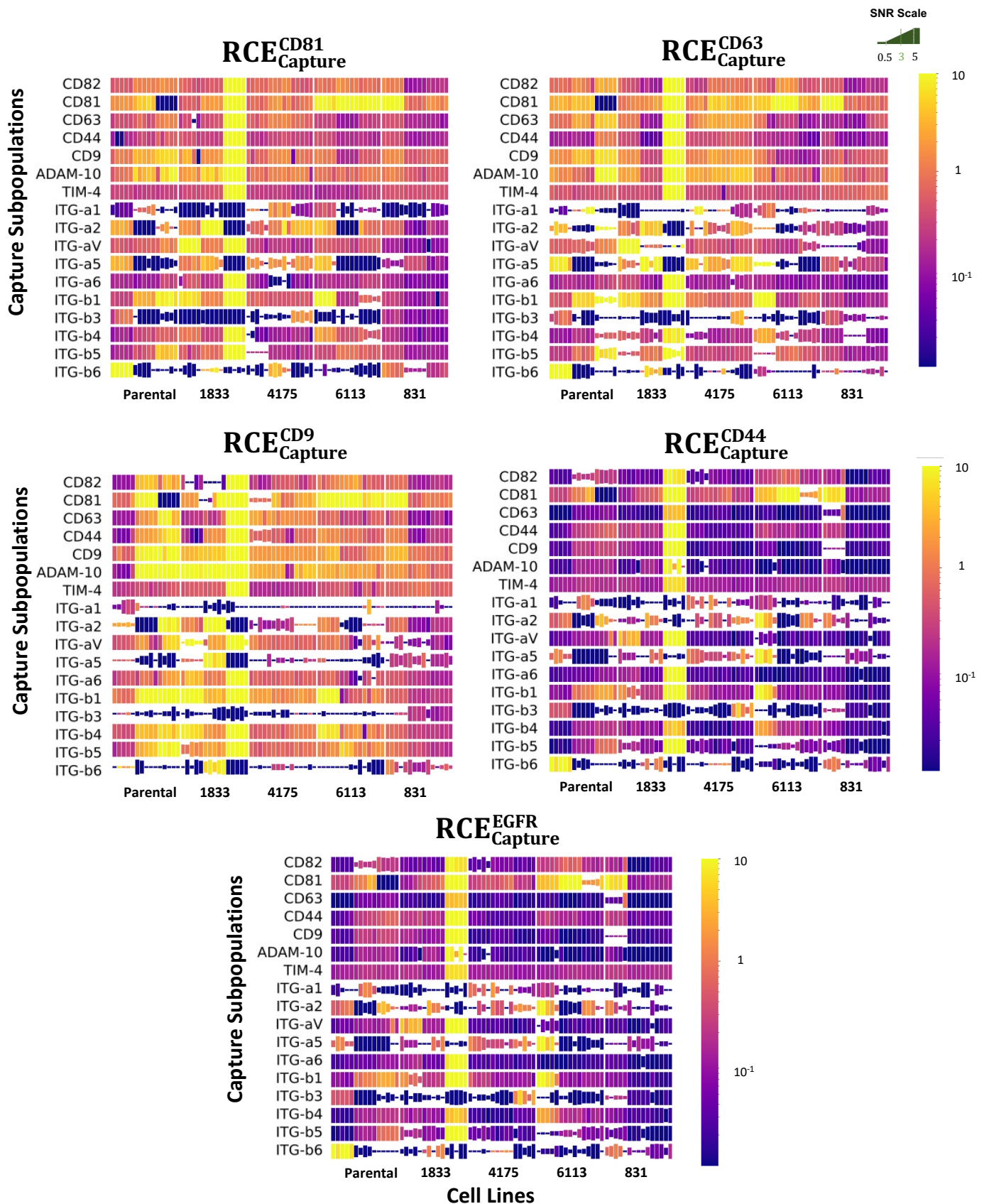
Supplementary Figure 1. Characterization of model EV population used in our experiments. **(A)** Size distribution of purified EV sample measured by TRPS. **(B)** Size distribution of purified EV sample measured by NTA. **(C)** TEM image of purified EV sample showcasing the EV's lipid bilayer and its distinctive cup-shape morphology.



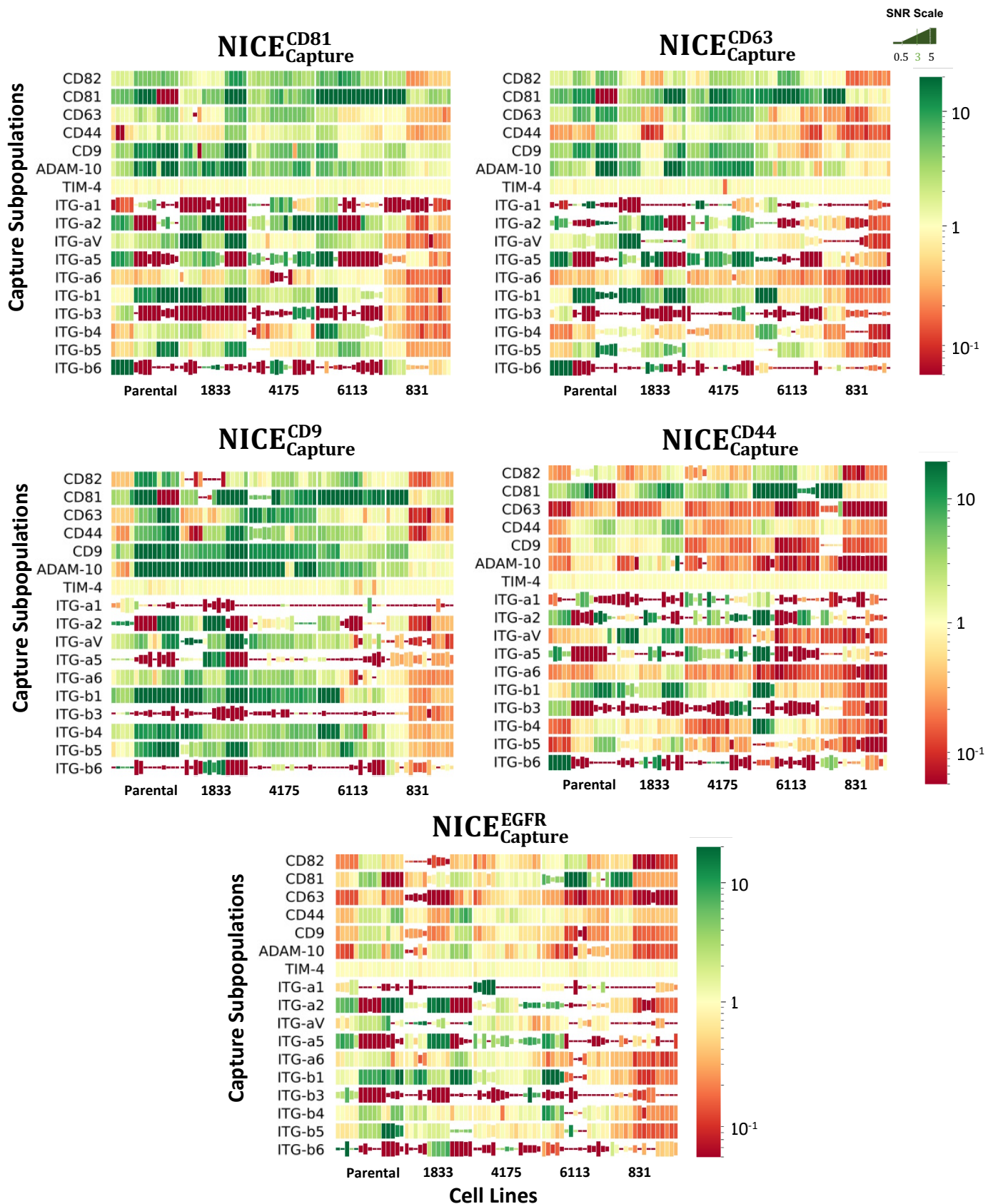
Supplementary Figure 2. Raw fluorescence intensity heatmaps of tetraspanin CD81, CD63 and CD9 expression profile of EV before normalization, captured subpopulations derived from breast cancer cell lines of varying metastatic potentials. Individual rectangles within the heatmap indicate 2 biological repeats with 5 technical repeats per biological repeat for a pooled $n = 10$. The SNR value for each individual measurement is reported as the height of the heatmap rectangle increasing from 0.5 – 5; smaller and larger SNR values are shown using the minimal and maximal value, respectively.



Supplementary Figure 3. Raw fluorescence intensity heatmaps of CD81, CD63, CD9, CD44 and EGFR expression profile of EV before normalization, captured subpopulations derived from triple negative breast cancer cell line MDA-MB-231 and its bone-, lung- and brain-organotropic sub-lines. Individual rectangles within the heatmap indicate 3 biological repeats with 5 technical repeats per biological repeat for a pooled $n = 15$. The SNR value for each individual measurement is reported as the height of the heatmap rectangle increasing from 0.5 – 5; smaller and larger SNR values are shown using the minimal and maximal value, respectively.



Supplementary Figure 4. RCE heatmaps of CD81, CD63, CD9, CD44 and EGFR expression profile of EV before normalization, captured subpopulations derived from triple negative breast cancer cell line MDA-MB-231 and its bone-, lung- and brain-organotropic sub-lines. Individual rectangles within the heatmap indicate 3 biological repeats with 5 technical repeats per biological repeat for a pooled $n = 15$. The SNR value for each individual measurement is reported as the height of the heatmap rectangle increasing from 0.5 – 5; smaller and larger SNR values are shown using the minimal and maximal value, respectively.



Supplementary Figure 5. NICE heatmaps of CD81, CD63, CD9, CD44 and EGFR expression profile of EV before normalization, captured subpopulations derived from triple negative breast cancer cell line MDA-MB-231 and its bone-, lung- and brain-organotropic sub-lines. Individual rectangles within the heatmap indicate 3 biological repeats with 5 technical repeats per biological repeat for a pooled $n = 15$. The SNR value for each individual measurement is reported as the height of the heatmap rectangle increasing from 0.5 – 5; smaller and larger SNR values are shown using the minimal and maximal value, respectively.